AD-755 854

ANALYTIC RADAR TARGET MODELING

R. Mittra, et al

Illinois University

Prepared for:

Army Missile Command

December 1972

UNCLASSIFIED

Security Classification

DOCUMENT CONTROL DATA - R & D

(Security classification of title, body of abstract and indexing annotation must be entered when the overall report is classified)

1. ORIGINATING ACTIVITY (Corporate author) Department of Electrical Engineering University of Illinois Urbana, Illinois 61801	2a. REPORT SECURITY CLASSIFICATION 2b. GROUP

3. REPORT TITLE

ANALYTIC RADAR TARGET MODELING

4. DESCRIPTIVE NOTES (Type of report and inclusive dates)

Final Report - 5 November 1971 to 5 November 1972

5. AUTHOR(S) (First name, middle initial, last name)

R. Mittra
S. W. Lee
C. A. Chuang

6. REPORT DATE December 1972	7a. TOTAL NO. OF PAGES 95	7b. NO. OF REFS 33
8a. CONTRACT OR GRANT NO DAAH01-72-C-0329 b. PROJECT NO. c. d.	9a. ORIGINATOR'S REPORT NUMBER(S) Antenna Laboratory Report No. 72-14 9b. OTHER REPORT NO(S) (Any other numbers that may be assigned this report) UILU-ENG-72-2558	

10. DISTRIBUTION STATEMENT

11. SUPPLEMENTARY NOTES	12. SPONSORING MILITARY ACTIVITY U. S. Army Missile Command Redstone Arsenal, Alabama 35809

13. ABSTRACT

This report studies the electromagnetic radar scattering parameters for a complex airborne target at high frequencies. The components of the target are modeled by simple geometrical shapes including ellipsoids, elliptical plates, ogives, and semi-infinite cylinders. Using ray-optics methods, the backscattered fields from each individual component are derived in terms of simple analytical functions. These are subsequently combined, in a consistent manner that takes into consideration the geometrical phase delay and shadowing effect, to yield the total scattered field from the target. Extensive numerical results are presented for the T-33 aircraft and the BQM-34A drone. A comparison of our theoretical computations with experimental data measured by a nanosecond short-pulsed radar reveals reasonably good agreement.

DD FORM 1 NOV 68 1473

UNCLASSIFIED

Security Classification

14. KEY WORDS	LINK A		LINK B		LINK C	
	ROLE	WT	ROLE	WT	ROLE	WT
Ray-optical method						
Radar cross section						
Backscattered field						
Glint						
Target-centered coordinate system						
Target modeling						

II

UILU-ENG-72-2558

ANTENNA LABORATORY REPORT NO. 72-14

ANALYTIC RADAR TARGET MODELING

by

R. Mittra
S. W. Lee
C. A. Chuang

Antenna Laboratory
Department of Electrical Engineering
University of Illinois at Urbana-Champaign

Contract No. DAAH01-72-C-0329

Final Report

5 November 1971 - 5 November 1972

December 1972

Contract Monitor: Dr. James Wright

Prepared for

U. S. Army Missile Command
Redstone Arsenal, Alabama 35809

III

TABLE OF CONTENTS

LIST OF FIGURES

Preceding page blank

LIST OF TABLES

1. INTRODUCTION

The purpose of this research is to determine the radar scattering characteristics of an airborne target with complex structure such as an airplane. Even though this subject matter has been studied extensively in the past twenty years [1, 2],there is no one method that is capable of producing efficient and accurate results under all conditions. One has to devise different computational schemes and employ different mathematical techniques which depend on factors such as the particular geometry of the target, the frequency range of interest, the acceptable error, and computation labor.

In the present study, we intend to develop a relatively simple analytical model of scattering from modern airplanes for the frequency range between 1 and 10 GH_z. Great precision of the theoretical model is not required since only the smoothed curves of the calculated data (e.g., medians over small angular region) will be of interest. Preliminary calculation is to be kept to a minimum because repeated calculations for a wide range of parameters will be performed for later statistical studies in the simulation of a particular radar system [2].

With the above objective in mind, we have searched the literature and evaluated the different techniques. It has been concluded that the ray-optical method [3-19]offers the best approach for the following reasons:

(i) This method is capable of handling target sizes that are large compared to the wavelength.

(ii) The ray-optical method yields a final result for the scattered field in terms of simple functions, thus allowing efficient numerical computation.

(iii) The ray-optics approach offers a convenient means for taking the shadowing effect into account. This is accomplished by first locating the scattering centers, or the bright points, and adding a simple logic in the program to indicate which of the bright points are in the shadow region for the aspect under consideration.

(iv) New developments in the ray-optical method enable one to treat three-dimensional problems[20-22], and to attack waveguide problems [23-27].

To solve the general scattering problem from a complex airborne target, we follow a recent study by Wright [2]. The essential steps and their appearance in this report are described below:

(i) The target is "resolved" into an ensemble of components, each of which can be geometrically approximated by a simple shape. This is discussed in Chapter 2.

(ii) The backscattered field from each component is calculated by the ray-optics method. Details of this step are given in Chapter 3.

(iii) The final step as presented in Chapter 4 is to combine the contributions from each component in a proper manner, taking into consideration the geometrical phase delay, the polarization, and the shadowing effect. Once the total backscattered field is obtained, the evaluation of various radar parameters, e.g., radar cross section, depolarization, and glint errors [28-30] can be accomplished by straightforward computations. Results from those computations and some comparison with experimental data are given in Chapter 5.

2. GENERAL DESCRIPTION

2.1 The Targets and Coordinate Systems

In this study we will consider two specific targets: the BQM-34A target drone (Figure 2.1), and the T-33 aircraft (Figure 2.2). The components of the targets will be modeled by perfectly conducting bodies having simple geometries which are described below:

(1) The ellipsoid (Figure 2.3), given by the equation

$$\frac{x^2}{a^2} + \frac{y^2}{b^2} + \frac{z^2}{c^2} = 1 \qquad (2.1)$$

will be used for modeling the fuselage and two wing pods.

(2) The elliptical plate (Figure 2.4), given by the equation

$$\frac{x^2}{a^2} + \frac{y^2}{b^2} = 1 , \quad \text{and } z = 0 \qquad (2.2)$$

will be used for modeling wings, horizontal and vertical tails.

(3) The open-ended , hollow, semi-infinite, elliptical cylinder (Figure 2.6), given by the equation

$$\frac{x^2}{a^2} + \frac{y^2}{b^2} = 1 , \quad \text{and } z \geq 0 \qquad (2.3)$$

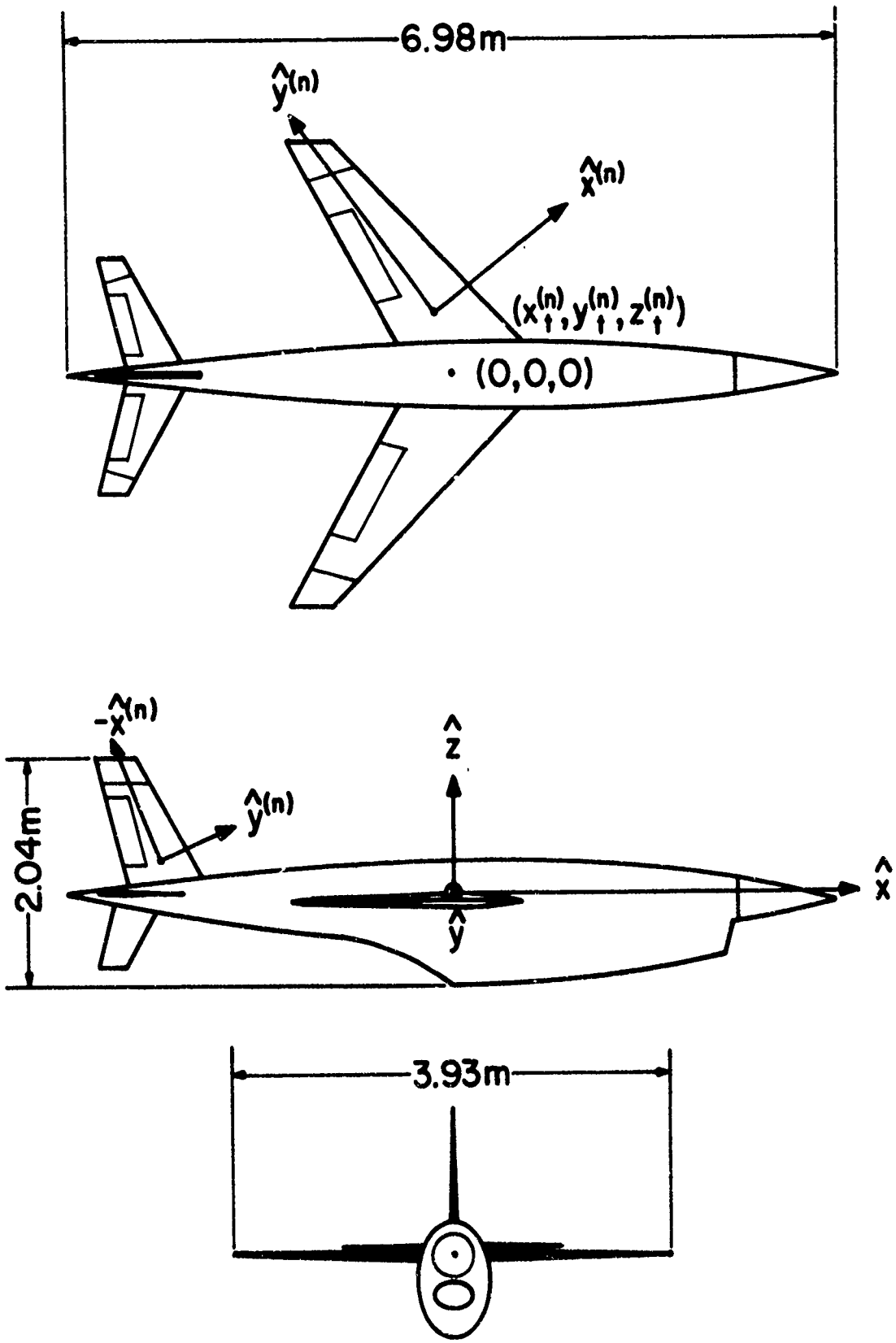

Figure 2.1. BQM-34A target drone

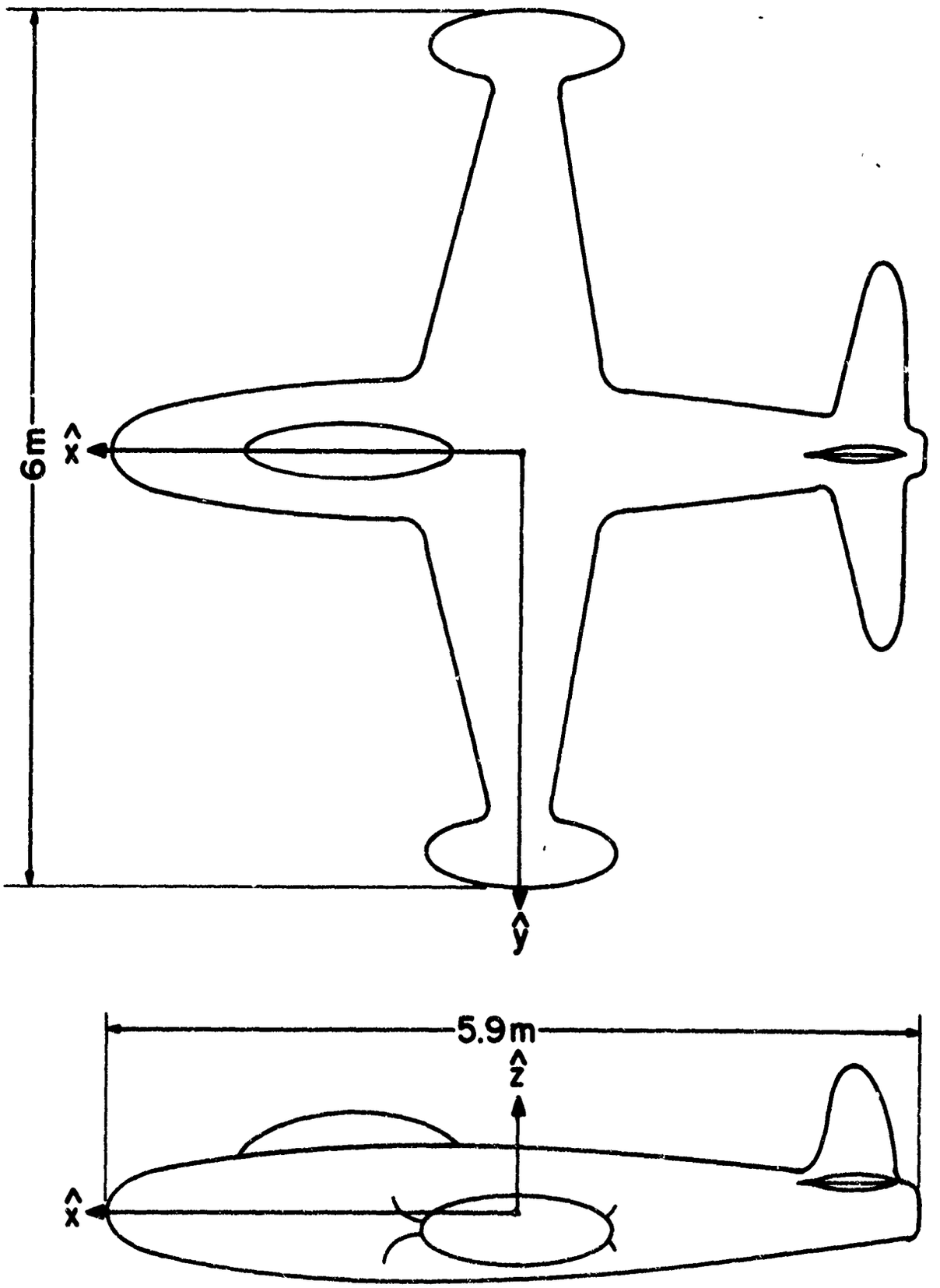

Figure 2.2. 1/2 scale T-33 aircraft

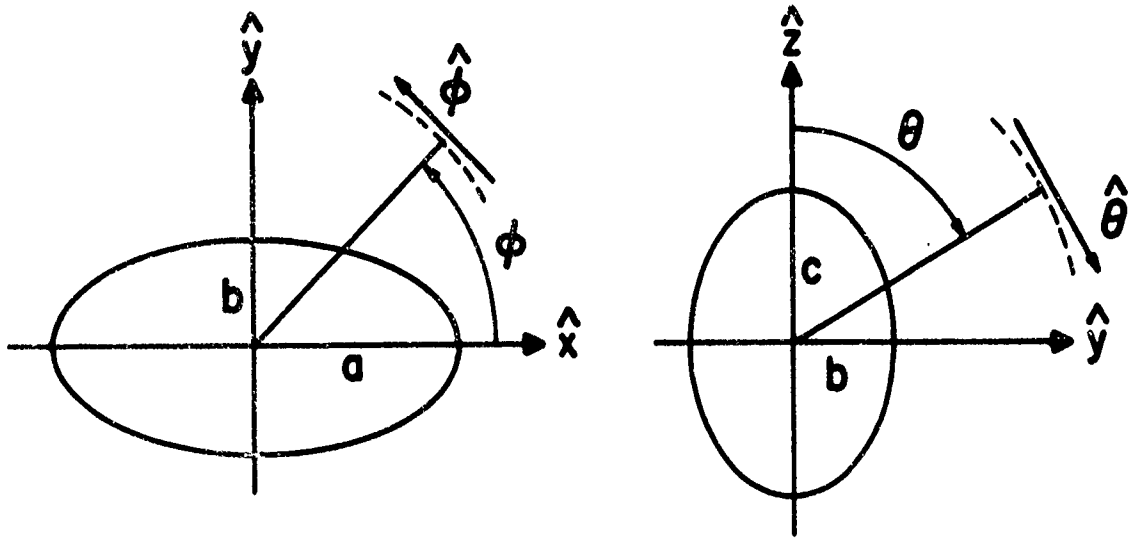

Figure 2.3. Geometry of an ellipsoid

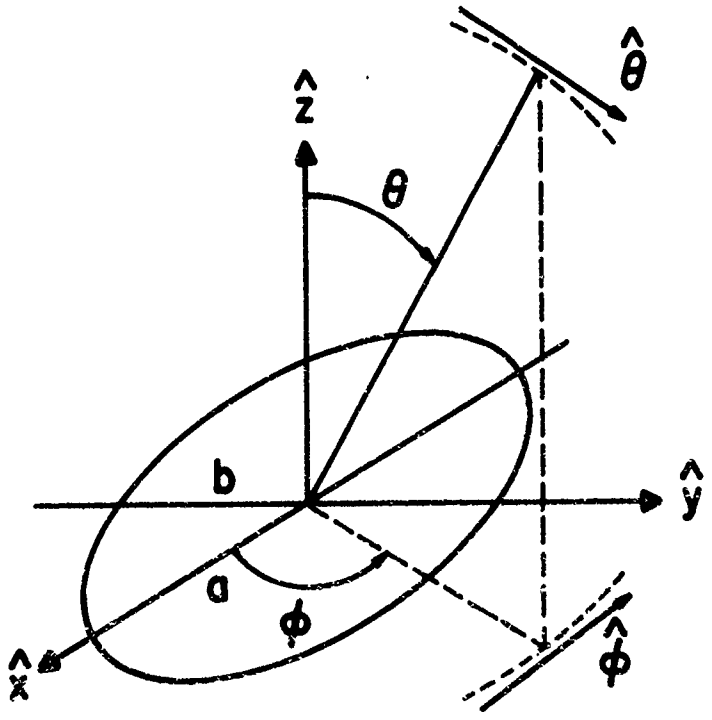

Figure 2.4. Geometry of an elliptical plate

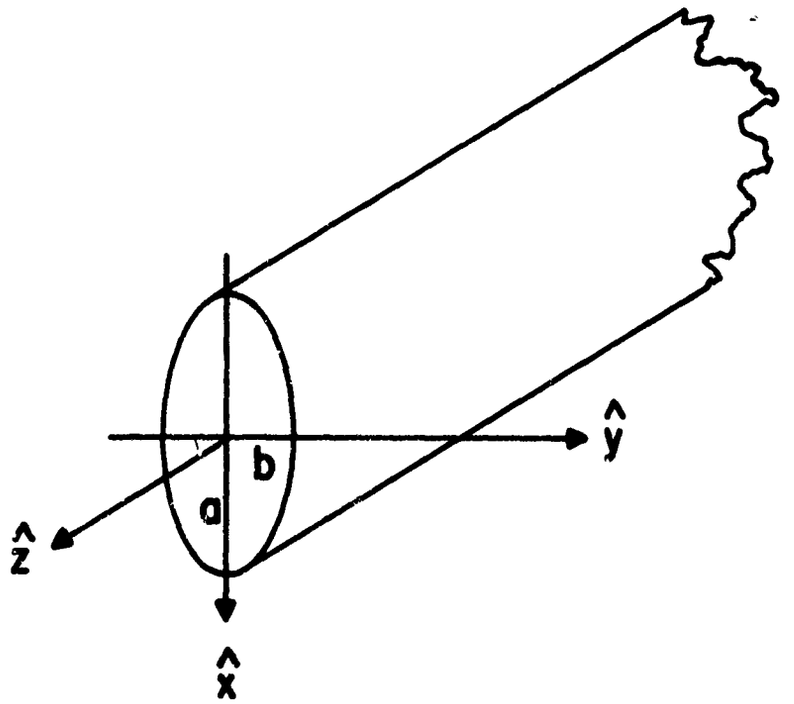

Figure 2.5. The open-end, hollow, semi-infinite elliptical cylinder

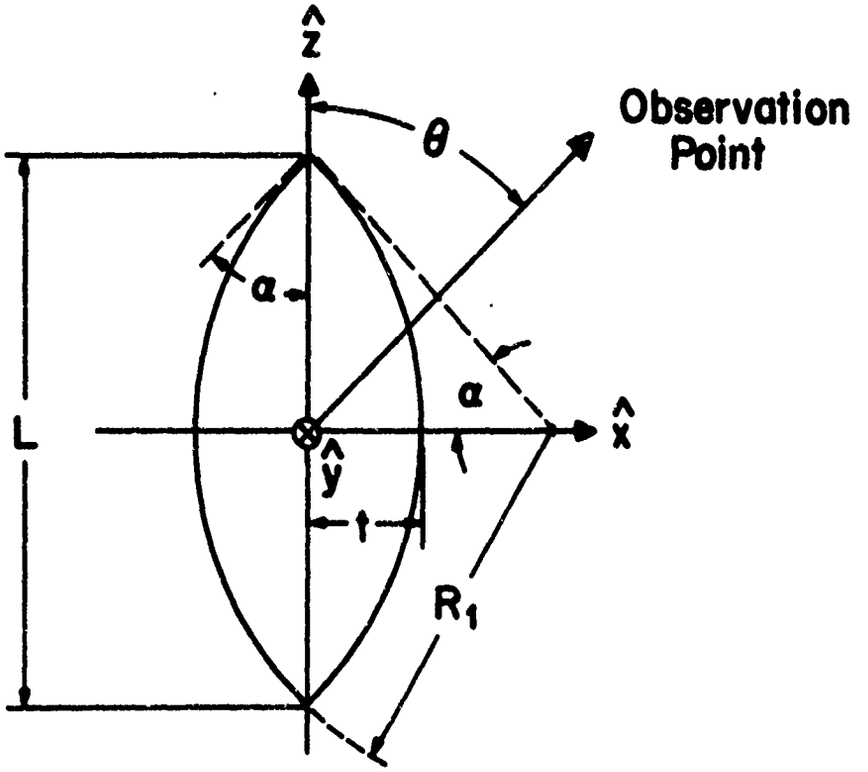

Figure 2.6. Geometry of the ogive

will be used for modeling jet engine intake and exhaust ducts.

(4) The ogive (Figure 2.7) is generated by rotating an arc of a circle of radius R_1 about a chord located a distance $R_1 - t$ from the center of the circle. The parameters (α, L) can be calculated from the relations:

$$\cos \alpha = 1 - \frac{t}{R_1} \tag{2.4}$$

$$L = 2 \sqrt{R_1^2 - (R_1^2 - t)^2} \quad . \tag{2.5}$$

Appropriately, truncated ogives will be used for simulating the terminations inside the engine intake and exhaust ducts.

To describe the relative position of each component, we will use two types of coordinate systems: the target-centered coordinate system, with variables denoted by (x,y,z); its origin is located at the center of the ellipsoid which models the fuselage; and its three axes in reference to the aircraft are oriented in the manner sketched in Figure 2.1. In general, there are as many local coordinate systems as the components that the aircraft are "resolved" into. We will denote the local coordinates by $(x^{(n)}, y^{(n)}, z^{(n)})$, with n = 1, 2, . . . N

and N being the total number of components. To describe a local coordinate in reference to the target-centered coordinate, the following six parameters may be used:

$(x_t^{(n)}, y_t^{(n)}, z_t^{(n)})$: Position of the origin of the nth local coordinate (see left wing of Figure 2.1 as an example)

$(\alpha^{(n)}, \beta^{(n)}, \gamma^{(n)})$: The angle $\alpha_t^{(n)}$ represents the rotation of the nth local coordinate about the z-axis of the target-centered coordinate, the angle $\beta^{(n)}$ about its new y-axis, and $\gamma^{(n)}$ about its new x-axis.

All rotations are defined in a right-handed sense. The explicit formulas for transforming variables from one coordinate system to another will be given in Section 4.1.

In Tables 2.1 and 2.2, the dimensions and the relative positions of components that have been used to model the two aircraft under consideration are presented. It should be mentioned that these dimensions presented in Tables 2.1 and 2.2 are not exact. For example, the data for T-33 aircraft were measured directly from a figure in reference [33]. Note that for the BQM-34A target drone, there are 12 components (N = 12) in total. Obviously, the detailed structure of

TABLE 2.1 COMPONENTS OF THE BQM-34A
(All dimensions are in meters)

Components	Approximated by	a	b	c	α (deg)	β (deg)	γ (deg)	x_t	y_t	z_t
Fuselage	ellipsoid	3.25	.352	.556	0	0	0	0.0	0.0	0.0
Left Wing	1/2 elliptical plate	.293	2.82	0.0	45	0	0	.614	0.0	-.3
Right Wing	1/2 elliptical plate	.293	2.82	0.0	-45	0	0	.614	0.0	-.3
Left Horizontal Stabilizer	1/2 elliptical plate	.235	1.41	0.0	45	0	0	-1.757	0.0	-.1
Right Horizontal Stabilizer	1/2 elliptical plate	.235	1.41	0.0	-45	0	0	-1.757	0.0	-.1
Vertical Stabilizer	1/2 elliptical plate	1.5	.322	0.0	0	45	90	-1.728	0.0	0.0
Left Wing Pod	ellipsoid	.6	.1	.3	0	0	0	-.41	1.46	-.35
Right Wing Pod	ellipsoid	.6	.1	.3	0	0	0	-.41	-1.46	-.35
Engine Intake Duct	hollow cylinder	.3	.2	0	90	0	90	2.2	0.0	0.0
Engine Exhaust Duct	hollow cylinder	.15	.15	0	90	0	-90	-3.0	0.0	0.0

Component	Approximated by	R_1	t	α	β	γ	x_t	y_t	z_t
Intake Termination	truncated ogive	.5	.085	0	0	90	1.7	0.0	0.0
Exhaust Termination	truncated ogive	.4	.086	0	180	90	-2.6	0.0	0.0

TABLE 2.2 COMPONENTS OF THE T-33 AIRCRAFT
(All dimensions are in meters)

Components	Approximated by	a	b	c	α	β	γ	x_t	y_t	z_t
Fuselage	ellipsoid	2.96	.381	.556	0	0	0	0.0	0.0	0.0
Left Wing	1/2 elliptical plate	.635	3.05	0.0	15	0	0	.614	0.0	-.3
Right Wing	1/2 elliptical plate	.635	3.05	0.0	-15	0	0	.614	0.0	-.3
Left Horizontal Stabilizer	1/2 elliptical plate	.305	1.14	0.0	15	0	0	-1.757	0.0	-.1
Right Horizontal Stabilizer	1/2 elliptical plate	.305	1.14	0.0	-15	0	0	-1.757	0.0	-.1
Vertical Stabilizer	1/2 elliptical plate	1.14	.305	0.0	0	45	90	-1.728	0.0	0.0
Left Wing Pod	ellipsoid	1.2	.15	.15	0	0	0	-.41	3.0	-.3
Right Wing Pod	ellipsoid	1.2	.15	.15	0	0	0	-.41	-3.0	-.3
Left Engine Intake Duct	hollow cylinder	.2	.2	0.0	90	0	90	.8	.4	0.0
Right Engine Intake Duct	hollow cylinder	.2	.2	0.0	90	0	90	.8	-.4	0.0
Engine Exhaust Duct	hollow cylinder	.35	.35	0.0	90	0	-90	-2.3	0.0	0.0

Components (Termination)	Approximated by	R_1	t	α	β	γ	x_t	y_t	z_t
Left Engine Intake	truncated ogive	.5	.085	0	0	90	.3	.4	0.0
Right Engine Intake	truncated ogive	.5	.085	0	0	90	.3	-.4	0.0
Engine Exhaust	truncated ogive	1.05	.53	0	180	90	-1.78	0.0	0.0

an aircraft is far more complex than that. The number N = 12 is chosen merely as a compromise between the accuracy of the modeling and the labor of computations. Our computer program is written in a such manner that if more accurate results are desired, several additional components may be added conveniently.

2.2 Scattering Parameters

One of the most important scattering parameters in a radar system is the backscattered radar cross section (RCS). For an incident time-harmonic plane wave with polarization

$$\vec{E}^{(i)} = \hat{e}_1 E^{(i)} \exp(-ik_o \hat{e}_3 \cdot \vec{r} - i\omega t) \tag{2.6}$$

where $(\hat{e}_1, \hat{e}_2, \hat{e}_3)$ form a right-hand orthonormal system. The backscattered field from a complex target, in general, can be written in the following form

$$\vec{E}^{(bs)} = (\hat{e}_1 E_1^{(bs)} + \hat{e}_2 E_2^{(bs)}) \exp(-ik_o \hat{e}_3 \cdot \vec{r} - i\omega t) \quad . \tag{2.7}$$

$E_1^{(bs)}$ represents the amplitude of the reflected wave with same polarization, while $E_2^{(bs)}$ is the amplitude of the reflected wave with cross polarization. Finally, the RCS is defined as

$$\sigma = 4\pi R^2 \frac{|E_1^{(bs)}|^2}{|E^{(i)}|^2} \tag{2.8}$$

where R is the radar range. Another definition used frequently is the RCS for the cross polarization,

$$\sigma_x = 4\pi R^2 \frac{|E_2^{(bs)}|^2}{|E^{(i)}|^2} \quad . \tag{2.9}$$

The algebraic sum of σ and σ_x is sometimes defined as the total RCS of the target, which is a measurement of the total reflected power with reference to the incident power.

In addition to RCS, the other parameters of interest in the present study are those describing the target-induced error in the radar system. While extensive discussions on the radar error can be found in the literature (e.g., Wright), we will present here only two definitions for the orthogonal errors caused by the distortion of the reflected wave front:

$$e_\theta = \frac{RP_\theta}{P_r} , \qquad e_\phi = \frac{RP_\phi}{P_r} \tag{2.10}$$

where e_θ and e_ϕ are known as the elevation and azimuth errors, respectively. (P_r, P_θ, P_ϕ) are the spherical components of the time-average power flow $\vec{p}$

of the backscattered field

$$\vec{p} = \mathrm{Re}(\vec{E}^{(bs)} \times \vec{H}^{(bs)}) \tag{2.11}$$

where Re is the real operator. In Chapter 5 the parameters σ, e_θ, and e_ϕ will be computed for each set of input conditions.

3. SCATTERED FIELD FROM INDIVIDUAL COMPONENTS

There are four basic geometries, namely, ellipsoid, elliptical plate, open-end elliptical cylinder, and ogive that have been used for modeling the aircraft of interest. In this section, the backscattered field from each of the geometries will be determined individually by the ray-optics method. In each case, the problem will be solved in its respective local coordinates $(x^{(n)},y^{(n)},z^{(n)})$.

Let us denote the incident wave by (with time factor $\exp(-i\omega t)$ supressed)

$$\vec{E}^{(i)} = (\hat{\theta}E_\theta + \hat{\phi}E_\phi)\exp(i\vec{k}\cdot\vec{r}) \qquad (3.1)$$

where $\vec{k} = (k,\theta,\phi)$ in the spherical coordinates, and (θ,ϕ) are the aspect angles. The backscattered field can be written in the form

$$\vec{E}^{(bs)} = (\hat{\theta}S_\theta + \hat{\phi}S_\phi)\frac{\exp(-i\cdot\vec{k}\cdot\vec{r})}{kr} \quad . \qquad (3.2)$$

Then the problem is to determine (S_θ,S_ϕ) for each geometry mentioned above. This will be carried out below.

3.1 The Ellipsoid

At high frequency, the main contribution from an ellipsoid (Figure 2.3)

to the backscattered field comes from the specular reflection at the point

$$x_S = \frac{a^2}{p} \sin\theta \cos\phi$$

$$y_S = \frac{b^2}{p} \sin\theta \sin\phi$$

$$z_S = \frac{c^2}{p} \cos\theta \qquad (3.3)$$

where

$$p = \sqrt{a^2 \sin^2\theta \cos^2\phi + b^2 \sin^2\theta \sin^2\phi + c^2 \cos^2\theta} \ ,$$

which is the so-called "scattering center" for the ellipsoid. In the discussion of the shadowing effect in Section 4.2, the position of the scattering center relative to other components of the aircraft determines the possiblity of a contribution to the total scattered field from the particular ellipsoid under consideration. Thus, the information in Equation (3.3) will be used later. The scattering amplitudes (S_θ, S_ϕ) have been worked out and the results are

$$S_\theta = -\frac{1}{2} E_\theta \left|\frac{kbc}{a}\right| \frac{1}{D^2} \exp(-i2kaD)$$

$$S_\phi = -\frac{1}{2} E_\phi \left|\frac{kbc}{a}\right| \frac{1}{D^2} \exp(-i2kaD) \qquad (3.4)$$

where

$$D = [\sin^2\theta \cos^2\phi + (b/a)^2 \sin^2\theta \sin^2\phi + (c/a)^2 \cos^2\theta]^{1/2} \quad . \qquad (3.5)$$

Since the ellipsoid is a smooth body, there is no cross polarization generated in the scattering process, and furthermore, the backscattered field is independent of the polarization of the incident wave.

3.2 The Elliptical Plate

The geometry of the elliptical plate is shown in Figure 3.1. If the minimum radius of curvature of the edge is large compared to the wavelength, i.e.,

$$k\, b^2/a \gg 1 \quad , \qquad (3.6)$$

then the far-field coefficients S_ϕ and S_θ for vertical ($E_\theta^{(i)} = 0$) and horizontal ($E_\phi^{(i)} = 0$) polarizations can be asymptotically expanded in a power series of $k^{-1/2}$. The dominant terms of these series come from

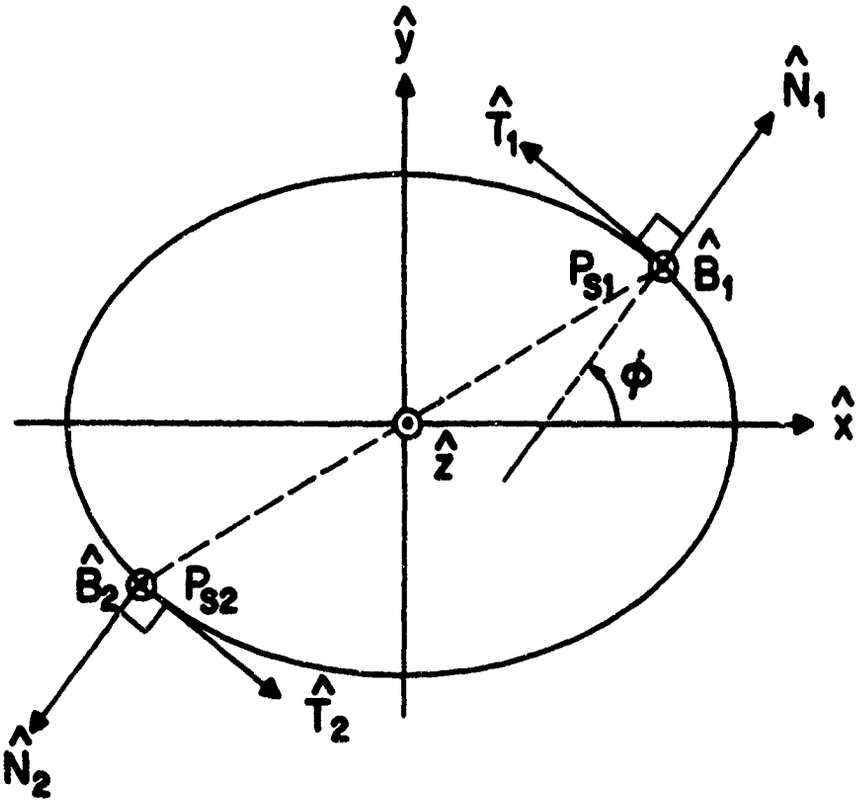

Figure 3.1. First-order scattering centers of the elliptical plate

optical rays which are backscattered from the scattering centers $P_{S1}(x_{S1},y_{S1},0)$ and $P_{S2}(x_{S2},y_{S2},0)$ on the edge of the plate. The coordinates of these two points are given by

$$x_{S1} = -x_{S2} = \frac{a}{A}\cos\phi$$

$$y_{S1} = -y_{S2} = \frac{b^2}{aA}\sin\phi$$

$$z_{S1} = z_{S2} = 0 \qquad (3.7)$$

where

$$A = [\cos^2\phi + (b/a)^2 \sin^2\phi]^{1/2} \quad . \qquad (3.8)$$

According to the geometrical theory of diffraction, the first-order scattered field at either of these points may be written in the form

$$\bar{E}^{(bs)} = \frac{e^{i\pi/4}}{\sqrt{2\pi k}} \Gamma \Delta \vec{e}^{i} \exp(ikr + i\Psi) \qquad (3.9)$$

where $\Gamma \sim$ the divergence factor

$\vec{e}^{i} \sim$ incident electrical field in terms of the base vectors $\hat{T}$, $\hat{B}$, and $\hat{N}$ (see Appendix A.1)

$\Psi \sim$ the phase delay.

The divergence factors Γ_1 and Γ_2 associated with the rays backscattered from P_{S1} and P_{S2} can be calculated by using Equations (A.3.1) and (A.3.2) in the Appendix, with $\rho' = \frac{b^3}{aA^3}$, $\beta = \pi/2$, $\hat{d} = -\hat{k} = \hat{x} \sin\theta \cos\phi + \hat{y} \sin\theta \sin\phi + \hat{z} \cos\theta$. The results are

$$\begin{bmatrix} \Gamma_1 \\ \\ \Gamma_2 \end{bmatrix} = \begin{bmatrix} 1 \\ \\ -1 \end{bmatrix} \frac{b}{r} A^{-3/2} (2a \sin\theta)^{-1/2} \quad . \tag{3.10}$$

The column vectors for the incident wave $(\vec{e}^i)_{P_{S1}}$, and $(\vec{e}^i)_{P_{S2}}$ are expressed in terms of the local base vectors $\hat{T}_1$, $\hat{N}_1$, $\hat{B}_1$ at P_{S1}, and $\hat{T}_2$, $\hat{N}_2$, $\hat{B}_2$ at P_{S2}, respectively. The local base vectors are illustrated in Figure 3.1, and are defined by

$$\hat{T}_1 = -\hat{T}_2 = -\hat{x} \sin\phi + \hat{y} \cos\phi$$

$$\hat{N}_1 = -\hat{N}_2 = \hat{x} \cos\phi + \hat{y} \sin\phi$$

$$\hat{B}_1 = \hat{B}_2 = -\hat{z} \quad . \tag{3.11}$$

For the incident field given in Equation (3.2), we have

$$(\vec{e}^i)_{P_{S1}} = \begin{pmatrix} E_\phi \\ E_\theta \cos\theta \\ E_\theta \sin\theta \end{pmatrix}$$

$$(\vec{e}^{i})_{P_{S2}} = \begin{pmatrix} -E_{\phi} \\ -E_{\theta} \cos\theta \\ E_{\theta} \sin\theta \end{pmatrix} \tag{3.12}$$

The diffraction matrices Δ_1 and Δ_2 for P_{S1} and P_{S2} are given by Equation (A.2.2), (A.2.5.), and (A.2.7) in the Appendix, with

$$\beta = \pi/2 \ ,$$

$$\alpha = \theta' = \theta \quad \text{for } \Delta_1 \ ,$$

and

$$\alpha = \theta' = -\theta \quad \text{for } \Delta_2 \ . \tag{3.13}$$

The diffraction angles α, θ' for P_{S1} and P_{S2} are illustrated in Figure 3.2. Thus, the diffraction matrices are

$$\Delta_1 = \frac{1}{2}\begin{pmatrix} -1 - \frac{1}{\sin\theta} & 0 & 0 \\ 0 & \left(1 + \frac{1}{\sin\theta}\right)\cos^2\theta & \left(1 - \frac{1}{\sin\theta}\right)\sin\theta\cos\theta \\ 0 & \left(1 - \frac{1}{\sin\theta}\right)\sin\theta\cos\theta & \left(1 - \frac{1}{\sin\theta}\right)\sin^2\theta \end{pmatrix} \tag{3.14}$$

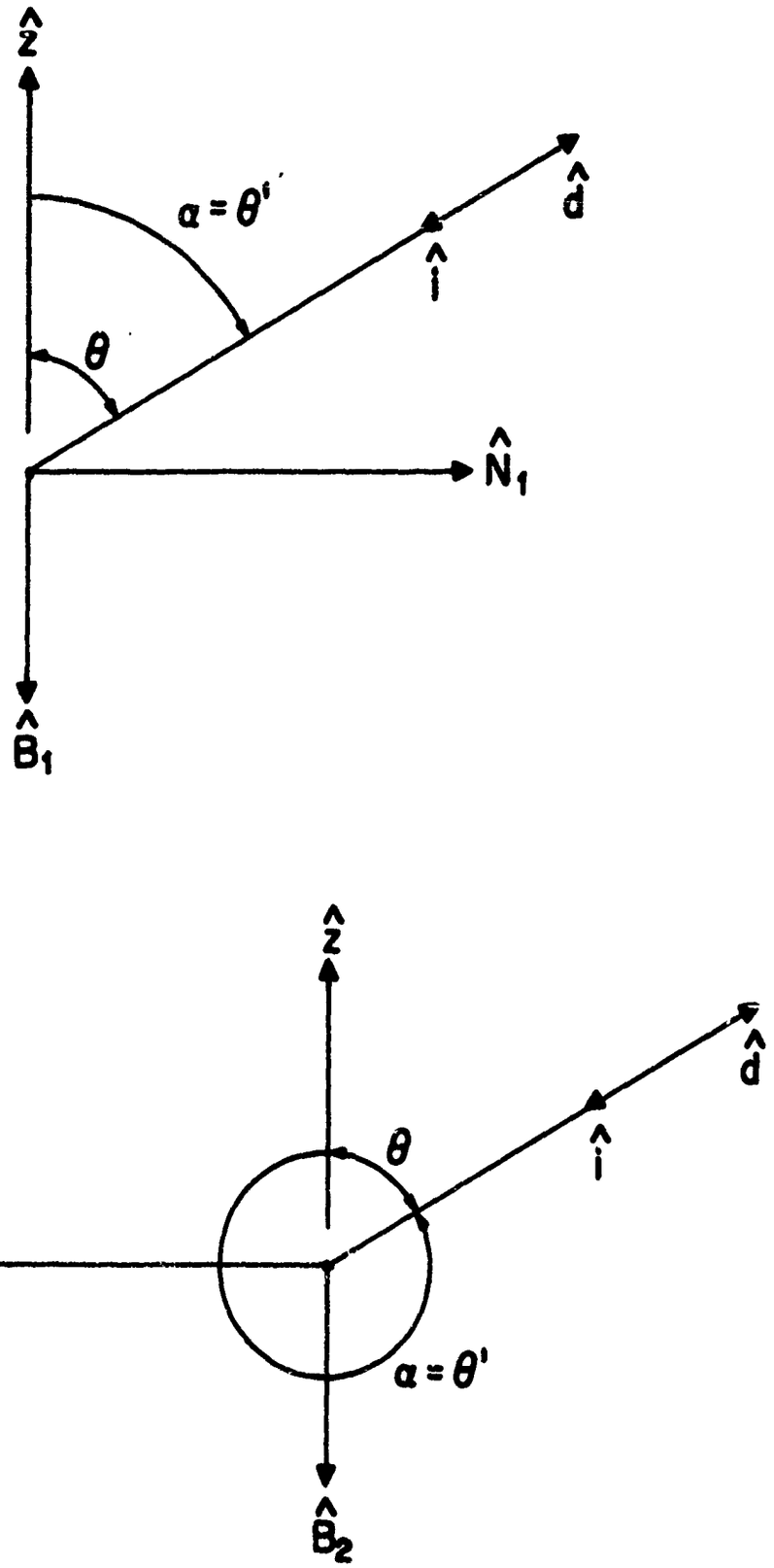

Figure 3.2. The diffraction angles for the elliptical plate

$$\Delta_2 = \frac{1}{2}\begin{pmatrix} -1 + \frac{1}{\sin\theta} & 0 & 0 \\ 0 & \left(1 + \frac{1}{\sin\theta}\right)\cos^2\theta & -\left(1 + \frac{1}{\sin\theta}\right)\sin\theta\cos\theta \\ 0 & -\left(1 + \frac{1}{\sin\theta}\right)\sin\theta\cos\theta & \left(1 + \frac{1}{\sin\theta}\right)\sin^2\theta \end{pmatrix} \tag{3.15}$$

The phase delay Ψ_1' and Ψ_2' for scattering fields at P_{S1} and P_{S2} are

$$\begin{bmatrix} \Psi_1' \\ \Psi_2' \end{bmatrix} = \begin{bmatrix} - \\ + \end{bmatrix} 2kA \sin\theta \quad . \tag{3.16}$$

Substituting Equations (3.10), (3.12), (3.14), (3.15), and (3.16) into Equation (3.9), we obtain $\vec{E}^{(bs)}$ in terms of the base vectors $\hat{T}_1$, $\hat{N}_1$, $\hat{B}_1$, $\hat{T}_2$, $\hat{N}_2$, and $\hat{B}_2$. Writing $\vec{E}^{(bs)}$ in the form of Equation (3.2), it follows that

$$S_{\substack{\phi \\ \theta}} = -\frac{b}{4a}\begin{pmatrix} E\phi \\ E\theta \end{pmatrix}\left(\frac{ka}{\pi \sin\theta}\right)A^{-3/2}\left[\left(1 \mp \frac{1}{\sin\theta}\right)\exp(i2kaA \sin\theta - i\,\pi/4)\right.$$

$$\left. + \left(1 \pm \frac{1}{\sin\theta}\right)\exp(-i2kaA \sin\theta + i\,\pi/4)\right], \quad (\theta \neq 0) \tag{3.17}$$

The above result does not apply when $\theta = 0$ and, therefore, it is not valid

when the direction of the incident wave is close to the z-axis. From a geometrical optics viewpoint, $\theta = 0$ defines a caustic where the diffracted rays from all points on the rim of the plate converge. To obtain the field in the caustic, we have to use techniques other than the ray-optics method.

For the exact case of $\theta = 0$, the present problem can be solved easily by using the physical optics method with the result

$$S_{\substack{\phi \\ \theta}} = \begin{pmatrix} +E\phi \\ -E\theta \end{pmatrix} \frac{1}{2} ab\, k^2 , \qquad (\theta = 0) \quad . \tag{3.18}$$

Since the first-order field obtained above is nonuniform in θ, we now introduce interpolating functions which yield results (3.17) and (3.18), as particular cases. A correct interpolation could be obtained by asymptotically expanding the exact solution of the scattering problem, if such a solution were available. A discussion similar to that performed by Keller for the circular edge would yield an axial correction factor containing a combination of Mathieu functions. For numerical purposes, it is preferable to introduce matching functions which are more easily calculated, such as Bessel functions.

We do not pretend that the formula thus produced is the correct interpolation, but only that it is sufficiently accurate for practical purposes.

A comparison between Equations (3.17), (3.18) and the corresponding results for a circular disk, as well as an inspection of the interpolation formula used for the circular disk, leads us to suggest the following expression

$$S_{\substack{\phi \\ \theta}} \approx \frac{ikb}{4A} \begin{pmatrix} E_\phi \\ E_\theta \end{pmatrix} \left[(\pm) \frac{J_1(2kaA \sin\theta)}{\sin\theta} - iJ_2(2kaA \sin\theta) \right] . \quad (3.19)$$

The above equation reduces to the result for the circular disk when $a = b$, to the physical result Equation (3.18) when $\theta = 0$, and to Equation (3.17) plus terms $O[(ka)^{-1/2}]$ when the argument of the Bessel functions is large with respect to a unit,

The result in Equation (3.17) is only the first-order solution for large ka. The higher-order terms were discussed in a separate report, but they will not be used in the present computations.

3.3 The Semi-Infinite Elliptical Cylinder

First let us consider the case when the cylinder is of circular shape, as shown in Figure 3.3. For the incident wave given in Equation (3.1),

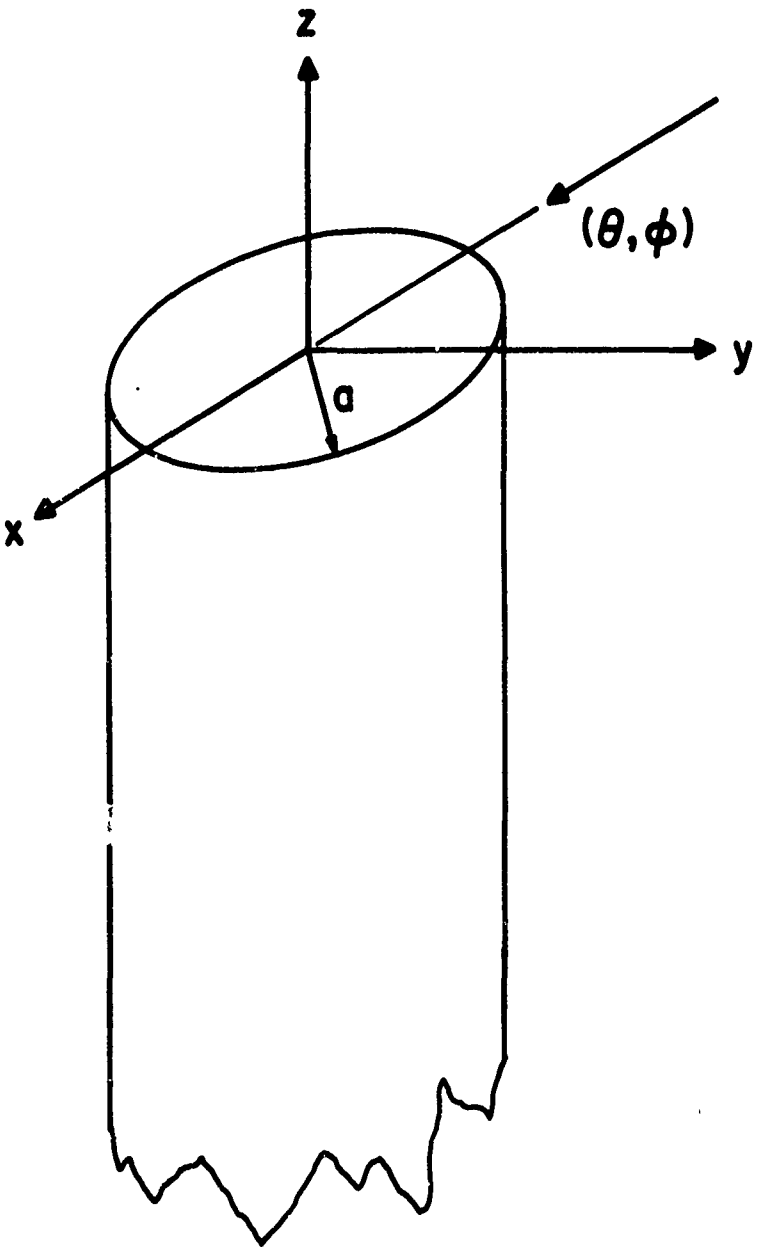

Figure 3.3. The semi-infinite circular cylinder

the exact solution can be obtained using the Wiener-Hopf technique [31,32]. Omitting the details, the final results are

$$S_\theta = \frac{E_\theta ka}{(\sin\frac{\theta}{2})^2} \sum_{n=-\infty}^{\infty} \frac{e^{in\phi} J_n^2(ka \sin\theta)}{L_n^2(ka \cos\theta)} \left[\frac{\sin^4\frac{\theta}{2}}{-\cos\theta} + \frac{\Delta_n^2}{1-\Delta_n^2}\right]$$

$$- \frac{iE_\phi 2ka}{\sin\theta} \sum_{n=-\infty}^{\infty} \frac{e^{in\phi} J_n(ka \sin\theta) J_n'(ka \sin\theta)}{L_n(ka \cos\theta) M_n(ka \sin\theta)} \frac{\Delta_n}{1-\Delta_n^2} \quad (3.20)$$

$$S_\phi = \frac{E_\phi ka}{(\cos\frac{\theta}{2})^2} \sum_{n=-\infty}^{\infty} \frac{e^{in\phi} J_n'(ka \sin\theta) J_n'(ka \sin\theta)}{M_n(ka \cos\theta) M_n(ka \cos\theta)} \left[\frac{\cos^4\frac{\theta}{2}}{\cos\theta} - \frac{\Delta_n^2}{1-\Delta_n^2}\right]$$

$$+ \frac{iE_\theta 2ka}{\sin\theta} \sum_{n=-\infty}^{\infty} \frac{e^{in\phi} J_n'(ka \sin\theta) J_n(ka \sin\theta)}{M_n(ka \cos\theta) L_n(ka \cos\theta)} \frac{\Delta_n}{1-\Delta_n^2} \quad . \quad (3.21)$$

In the above equations, the following notation has been used

$$\Delta_n = \frac{n}{2ka} \frac{L_n(ka)}{M_n(ka)} \quad . \quad (3.22)$$

The functions $L_n(\omega)$ and $M_n(\omega)$ are analytic in the upper half of the complex ω-plane and are defined by

$$L_n(\omega)\, L_n(-\omega) = \pi\lambda\, J_n(\lambda)\, H_n^{(1)}(\lambda)$$

$$M_n(\omega)\, M_n(-\omega) = \pi\lambda\, J_n'(\lambda)\, H_n^{(1)'}(\lambda) \quad (3.23)$$

where

$$\lambda = \sqrt{(ka)^2 - \omega^2} , \qquad \mathrm{Im}\lambda > 0 \text{ for } \mathrm{Im}k > 0 \ .$$

The above results are too complicated to be useful. (Note that $L_n(\omega)$, for example, is explicitly given by an infinite integral[30]). For high frequencies, we may use the approximations

$$L_n(\omega), M_n(\omega) \to 1 , \qquad \text{as } ka \to \infty \ . \tag{3.24}$$

Then the results in Equations (3.20) and (3.21) can be considerably simplified

$$S_\theta = \frac{-E_\theta ka}{\cos\theta}\left[\sin^2\left(\frac{\theta}{2}\right) J_0(2ka\sin\theta) + \sin\theta\cos^2\left(\frac{\theta}{2}\right)\frac{J_1(2ka\sin\theta)}{2ka\sin\theta}\right] \tag{3.25}$$

$$S_\phi = \frac{-E_\theta ka}{\cos\theta}\cos^2\left(\frac{\theta}{2}\right) J_1'(2ka\sin\theta) \ . \tag{3.26}$$

The above simple formulas are valid for all θ except for $\theta \approx \pi/2$. The plane $\theta = \pi/2$ defines the shadow boundary for the specularly reflected wave from the cylinder, and the expressions for (S_θ, S_ϕ) as given in (3.20) and (3.21) no longer hold since they were derived from simple saddle-point integration. Fortunately in the present application, we are only interested in the case with $\theta = 0$ (head-on incidence) and its

immediate neighborhood ,i.e., $\theta < \pi/4$. Thus this shortcoming of the formulas at $\theta = \pi/2$ has no effect in the later computations.

Because of its application to the radar return calculation from an engine intake, the problem of scattering by a semi-infinite cylinder has been studied extensively in the past fifteen years. For the first time, a simple analytical formula has been derived, i.e., Equations (3.25) and (3.26). Bowmain in 1970 gave a similar result except that his expression for S_θ contains only the first form of (3.25) and therefore is not valid for $\theta = 0$ and its neighborhood. For ka sin $\theta >> 1$, the results in (3.25) and (3.26) are reduced to

$$S_{\theta}^{\phi} \sim -\frac{1}{2}\begin{pmatrix} E\phi \\ E\theta \end{pmatrix}\left(\frac{ka}{\pi \sin\theta}\right)^{\frac{1}{2}}\left(1 \pm \frac{1}{\cos\theta}\right)\cos(2\,ka\sin\theta - \pi/4) \qquad (3.27)$$

which agree with the ray-optics expression derived by Ross in 1967. As is well-known, the ray-optics expression is not valid in the caustic region ($\theta \simeq 0$) which is precisely the case of interest in the present study.

The cylinder considered above has a circular shape. By proper scaling, an approximate formula for an elliptical cylinder (with a major

axis a and minor axis b as shown in Figure 2.5), can be derived. The scaling factor we have selected is the one between a circular plate and an elliptical plate; it has been rigorously determined [3,4]. In terms of the backscattered field, the use of the scaling factor leads to this result:

$$\vec{E}^{(bs)}(\text{elliptical}) = \left(\frac{b}{a}\right)^{1/2} \vec{E}^{(bs)}(\text{circular with radius } aA) \tag{3.28}$$

where (aA) can be considered as the "effective radius" for an elliptical cylinder with

$$A = \sqrt{\cos^2 \phi + (b/a)^2 \sin^2 \phi} \tag{3.29}$$

and ϕ is the azimuthal angle of the incident plane wave.

3.4 The Ogive

The geometry of an ogive is shown in Figure 2.6. The scattered field from the ogive can be obtained by applying the optics approach [1]. For the present problem, we are only interested in the region $(90^\circ - \alpha) < \theta \leq 90^\circ$, where the scattering amplitudes are given by

$$S_{\theta}^{\phi} = -\left(\frac{E_\phi}{E_\theta}\right)\frac{R_1}{2}\left(1 - \frac{R_1 - t}{R_1 \sin\theta}\right)^{1/2} . \tag{3.30}$$

4. TOTAL SCATTERED FIELD

4.1 Transformations of Coordinates

In the previous chapter, the backscattered fields from individual components were found and the final results were expressed in terms of their respective local coordinates. To combine them properly for the total scattered field, those results have to be transformed so that they have a common reference, namely the target-centered coordinate system. Such a transformation is straightforward but quite tedious, and a small mistake may crucially affect the final result. Therefore, we will discuss various transformations in explicit detail. Our choice of coordinate systems is essentially the same as that used by Wright except for some small variations.

For the target-centered coordinate system (TCS), the x axis is along the longitudinal direction of the aircraft with the positive direction pointing from the tail to the head of the aircraft (see Figure 2.1). The positive y axis is directed to the left side of the fuselage, and the z axis is along the vertical direction of the aircraft.

The other coordinate systems of interest are the local coordinate

systems (LCS) which are assigned to each component of the target. The left wing is taken as the example which illustrates the LCS. The left wing is approximated by a half of an elliptical plate. The origin of the coordinate system is located at the center of symmetry of the ellipse, and the x and y axes are the axes of symmetry in which the y axis is the major axis pointing to the left side of the target (See Figure 4.1). The LCS's for the rest of the components are assigned in a similar manner. The LCS is obtained by making a translation and three successive rotations from TCS. Let x_t, y_t, and z_t be the coordinates of the origin of the local coordinate system referred to target-centered system, α be the rotation angle of the LCS about its z axis, β be the rotation angle about its new y axis, and γ be the rotation angle about its new x axis (See Figure 4.1). All three notations are defined in a right-hand sense. Let x, y, z be the coordinates of a point in the TCS, and x', y', z' be the coordinates of this point in the local coordinate system. Then the coordinates of the point are related by the following transformations:

$$\begin{bmatrix} x' \\ y' \\ z' \end{bmatrix} = \begin{bmatrix} t_{11} & t_{12} & t_{13} \\ t_{21} & t_{22} & t_{23} \\ t_{31} & t_{32} & t_{33} \end{bmatrix} \begin{bmatrix} x - x_t \\ y - y_t \\ z - z_t \end{bmatrix} \qquad (4.1)$$

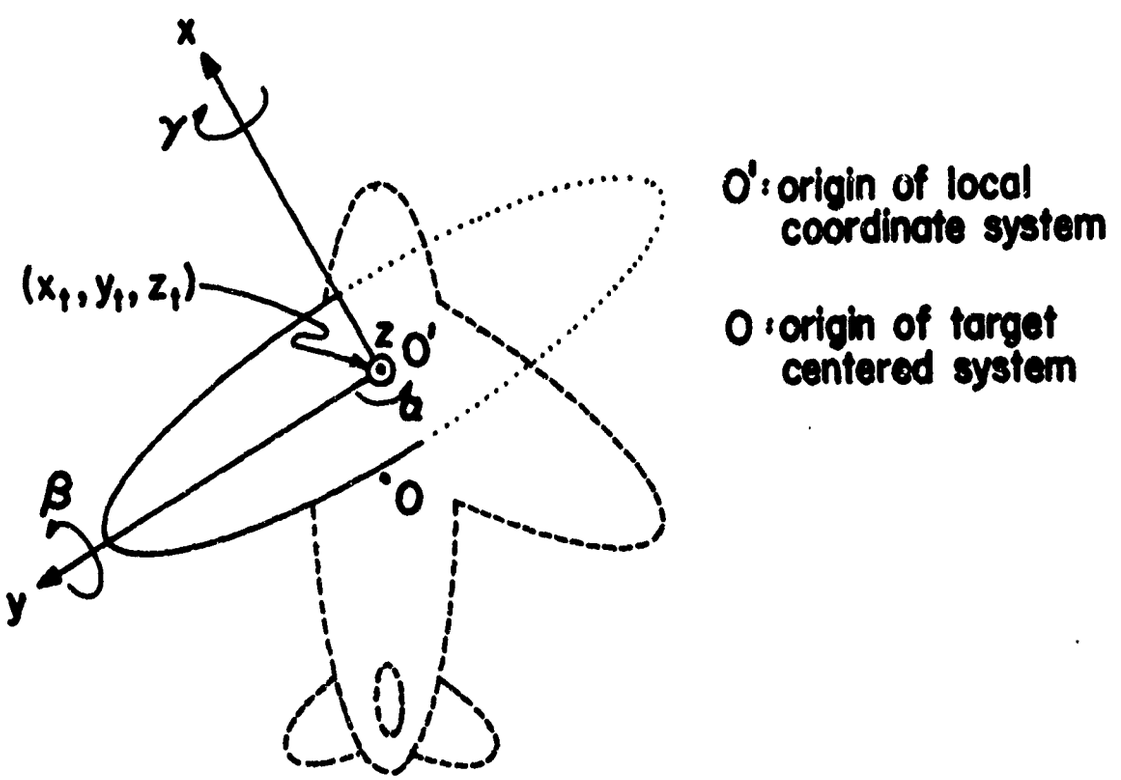

Figure 4.1. Local coordinates for the left wing

$$\begin{bmatrix} x \\ y \\ z \end{bmatrix} = \begin{bmatrix} t_{11} & t_{21} & t_{31} \\ t_{12} & t_{22} & t_{32} \\ t_{13} & t_{23} & t_{33} \end{bmatrix} \begin{bmatrix} x \\ y \\ z \end{bmatrix} + \begin{bmatrix} x_t \\ y_t \\ z_t \end{bmatrix} \qquad (4.2)$$

where

$$t_{11} = \cos \alpha \cos \beta$$

$$t_{12} = \sin \alpha \cos \beta$$

$$t_{13} = - \sin \beta$$

$$t_{21} = - \sin \alpha \cos \gamma + \cos \alpha \sin \beta \sin \gamma$$

$$t_{22} = \cos \alpha \cos \gamma + \sin \alpha \sin \beta \sin \gamma$$

$$t_{23} = \cos \beta \sin \gamma$$

$$t_{31} = \sin \alpha \sin \gamma + \cos \alpha \sin \beta \cos \gamma$$

$$t_{32} = - \cos \alpha \sin \gamma + \sin \alpha \sin \beta \cos \gamma$$

$$t_{33} = \cos \beta \cos \gamma \quad . \qquad (4.3)$$

In the above transformation, the three successive rotations α, β, and γ have to be made in the order as stated; that is, α first, β second, and γ third. The corresponding values of x_t, y_t, z_t, α, β, and γ for components of our targets are listed in Tables 2.1 and 2.2.

Any point in space can be given in spherical coordinates by (R,θ,ϕ) with respect to some coordinate system. The angles θ and ϕ which are the spherical coordinates of the radar in the TCS are usually referred to as the aspect angles. The aspect angles are shown in Figure 4.2. The scattered field for the nth component of the targets can be calculated when the aspect angles $\theta^{(n)}$, $\phi^{(n)}$ for the component in the LCS are known. For the given aspect angles θ and ϕ in TCS, the aspect angles $\theta^{(n)}$, $\phi^{(n)}$ in the nth LCS can be calculated as follows

$$\phi^{(n)} = \arctan \frac{y'_o}{x'_o} \tag{4.4}$$

and

$$\theta^{(n)} = \arctan \frac{\sqrt{(x'_o)^2 + (y'_o)^2}}{z'_o} \tag{4.5}$$

where

$$\begin{bmatrix} x'_o \\ y'_o \\ z'_o \end{bmatrix} = \begin{bmatrix} t_{11} & t_{12} & t_{13} \\ t_{21} & t_{22} & t_{23} \\ t_{31} & t_{32} & t_{33} \end{bmatrix} \begin{bmatrix} \cos\phi \sin\theta \\ \sin\phi \sin\theta \\ \cos\theta \end{bmatrix} . \tag{4.6}$$

The transformation in Equation (4.6) is valid when

$$R >> (x_t^2 + y_t^2 + z^2)^{1/2} \tag{4.7}$$

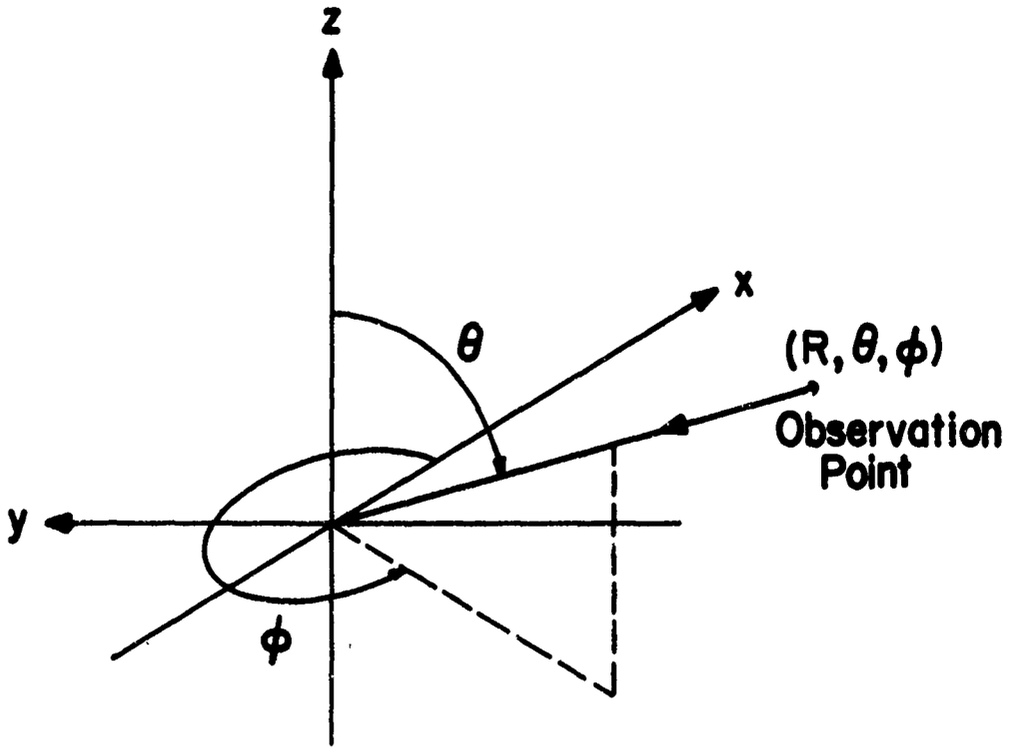

Figure 4.2. Aspect angles w.r.t. target centered coordinates

where R is the range of the radar referred to the TCS.

In calculating the backscattered field from each component, it is necessary to transform the incident field given in the TCS to that in the LCS, and also to transform the backscattered field in the reverse direction.

For an incident plane wave in Equation (3.1), the electric field amplitude is expressed by a column vector

$$\bar{\bar{E}}^i = \begin{bmatrix} 0 \\ E_\theta \\ E_\phi \end{bmatrix} \tag{4.8}$$

which is written in terms of base vectors in spherical coordinates.

In the nth LCS, it becomes

$$\bar{\bar{E}}^{i(n)} = U\ T\ S\ \bar{\bar{E}}^i \tag{4.9}$$

where

$$S = \begin{bmatrix} \sin\theta\cos\phi & \cos\theta\cos\phi & -\sin\phi \\ \sin\theta\sin\phi & \cos\phi\sin\phi & \cos\phi \\ \cos\theta & -\sin\theta & 0 \end{bmatrix} \tag{4.10}$$

$$T = \begin{bmatrix} t_{11} & t_{12} & t_{13} \\ t_{21} & t_{22} & t_{23} \\ t_{31} & t_{32} & t_{32} \end{bmatrix} \tag{4.11}$$

with t_{ij}'s as in Equation (4.3) and

$$U = \begin{bmatrix} \sin\theta^{(n)} \cos\phi^{(n)} & \sin\theta^{(n)} \sin\phi^{(n)} & \cos\theta^{(n)} \\ \cos\theta^{(n)} \cos\phi^{(n)} & \cos\theta^{(n)} \sin\phi^{(n)} & -\sin\theta^{(n)} \\ -\sin\phi^{(n)} & \cos\phi^{(n)} & 0 \end{bmatrix} . \tag{4.12}$$

Note that the translation of the origins from the target centered coordinates is neglected here. Similarly, for a given $\vec{E}^{(bs),(n-\ell)}$ in LCS, the $\vec{E}^{(bs),(n)}$ in TCS is given by

$$\vec{E}^{(bs),(n)} = W\, S'\, T'\, U'\, \vec{E}^{(bs),(n-\ell)} \tag{4.13}$$

where U', T', S' are transposes of matrices U, T, S, respectively, and

$$W = \begin{bmatrix} 1 & W_1 & W_2 \\ 0 & 1 & 0 \\ 0 & 0 & 1 \end{bmatrix} \tag{4.14}$$

with

$$W_1 = -x_t \cos\theta \cos\phi - y_t \cos\theta \sin\phi - z_t \sin\theta$$

$$W_2 = -x_t \sin\phi + y_t \cos\phi \quad . \tag{4.15}$$

The matrix W takes into consideration the amplitude shift of the scattered field of the nth component caused by the origin shift of its LCS from the origin of the TCS. The phase shift of the scattered field of the component caused by the origin shift is given by

$$\phi^{(n)} = -2k(x_t \sin\theta \cos\phi + y_t \sin\theta \sin\phi + z_t \cos\theta) . \tag{4.16}$$

In Equations (4.15) and (4.16), the point (x_t, y_t, z_t) represents the position of the LCS origin referred to the TCS, and the angles θ and ϕ are the aspect angles in the TCS.

4.2 Shadowing Effects

In the present study, we used the ray-optics approach for the determination of the scattered field except for the case of caustics; the scattered fields are generated exclusively from the scattering at the "scattering centers." For a given incident angle, a scattering center of a component may or may not be shadowed by other components of

the aircraft. If it is shadowed, there is no contribution from that scattering center to the total scattered field; otherwise, its entire contribution will be included. To account for the "all-or-nothing" shadowing effect, we will introduce a simple modulation function for each component of the aircraft.

$$G^{(n)}(\theta,\phi) = \begin{cases} 1 & \text{if } (\theta,\phi) \text{ is in the visible region of the component} \\ 0 & \text{if } (\theta,\phi) \text{ is in the shadow region} \end{cases} \tag{4.17}$$

where θ, ϕ are the aspect angles in the TCS. As an example, the shadowed and visible regions of the left wing of the BQM-34A target drone are illustrated in Figure 4.3 when $\theta = 90^{\circ}$. For the incident angle ϕ greater than -15° and less than 100°, the left wing is in the visible region [$G^{(n)}(\theta,\phi) = 1$]; otherwise, it is in the shadow region [$G^{(n)}(\theta,\phi) = 0$]. The shadow and visible regions of the components of our targets are listed in Tables 4.1 and 4.2.

4.3 Computational Procedure

The scattering parameters of interest, as functions of aspect angles, are computed by using the following procedure:

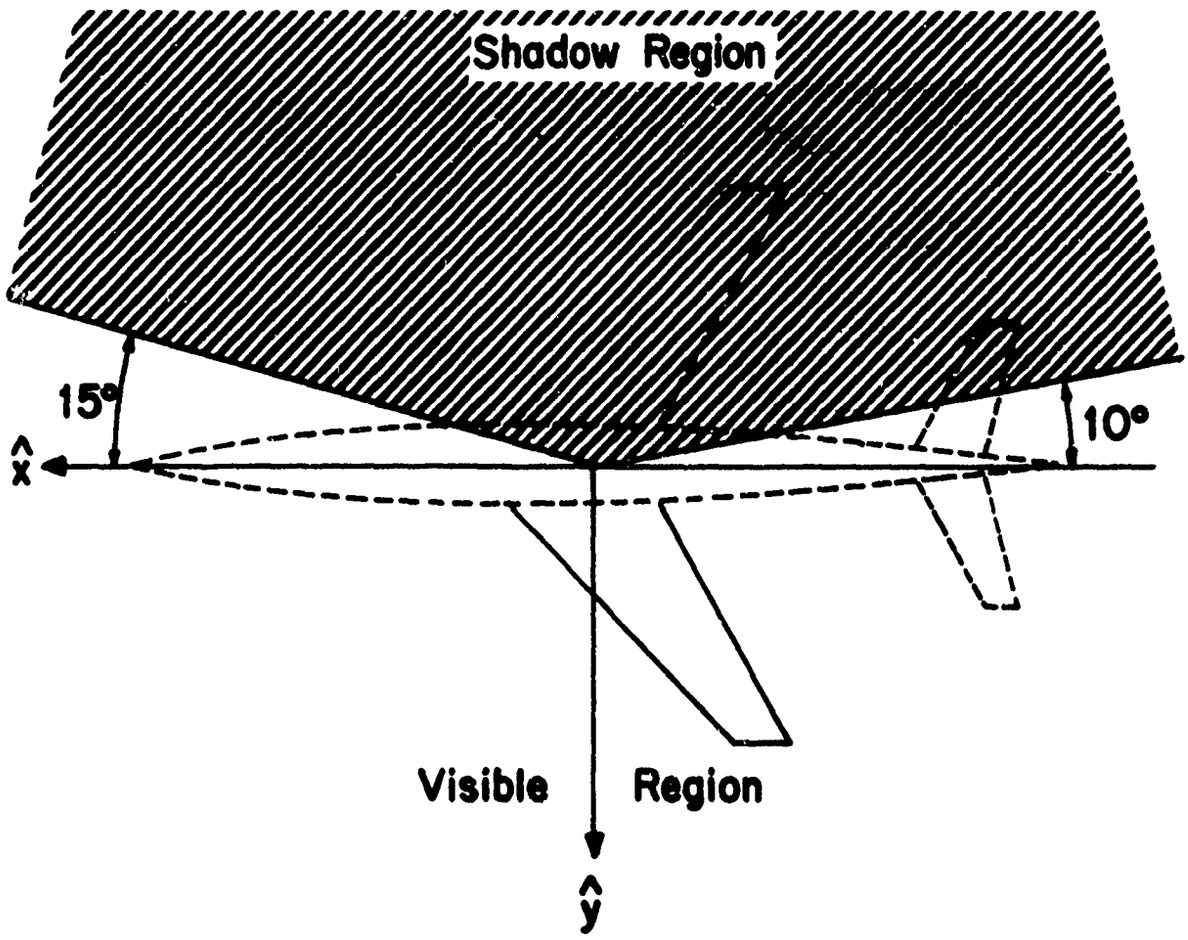

Figure 4.3. The shadowing region of the left wing of BQM-34A target drone

TABLE 4.1 SHADOWING REGIONS OF COMPONENTS OF THE BQM-34A
(All angles are in degrees)

Component	visible region		shadow region	
	$85 \leq \theta \leq 95$	$0 \leq \theta < 85$ or $95 < \theta \leq 180$	$85 \leq \theta \leq 95$	$0 \leq \theta < 85$ or $95 < \theta \leq 180$
Left Wing	$-15 \leq \phi \leq 190$	all ϕ	$190 < \phi < -15$	—
Right Wing	$170 \leq \phi \leq 15$	all ϕ	$15 < \phi < 170$	—
Left Horizontal Stabilizer	$90 \leq \phi \leq 210$	all ϕ	$210 < \phi < 90$	—
Right Horizontal Stabilizer	$150 \leq \phi \leq 270$	all ϕ	$270 < \phi < 150$	—
Left Wing Pod	$-25 \leq \phi \leq 200$	all ϕ	$200 < \phi < -25$	—
Right Wing Pod	$160 \leq \phi \leq 25$	all ϕ	$25 < \phi < 160$	—

Component		visible region		shadow region	
Fuselage		all (θ,ϕ)		—	
Vertical Stabilizer		$0 \leq \theta \leq 90$ all ϕ	$90 < \theta < 180$ $135 \leq \phi \leq 225$	—	$90 < \theta < 180$ $225 < \phi < 135$
Engine Intake	duct	$\lvert\phi\rvert \leq 40$ and $\lvert\theta - 90\rvert \leq 40$		$\lvert\phi\rvert > 40$ or $\lvert\theta - 90\rvert > 40$	
	termination	$\lvert\phi\rvert \leq 30$ and $\lvert\theta - 90\rvert \leq 20$		$\lvert\phi\rvert > 30$ or $\lvert\theta - 90\rvert > 20$	
Engine Exhaust	duct	$\lvert\phi\rvert \leq 40$ and $\lvert\theta - 90\rvert \leq 40$		$\lvert\phi\rvert > 40$ or $\lvert\theta - 90\rvert > 40$	
	termination	$\lvert\phi\rvert \leq 35$ and $\lvert\theta - 90\rvert \leq 30$		$\lvert\phi\rvert > 35$ or $\lvert\theta - 90\rvert > 30$	

TABLE 4.2 SHADOWING REGIONS OF COMPONENTS OF THE T-33
(All angles are in degrees)

Component	Visible Region		Shadow Region	
	$85 \leq \theta \leq 95$	$0 \leq \theta < 85$ or $95 < \theta \leq 180$	$85 \leq \theta \leq 95$	$0 \leq \theta < 85$ or $95 < \theta \leq 180$
Left Wing	$-25 \leq \phi \leq 195$	all ϕ	$195 < \phi < -25$	———
Right Wing	$165 \leq \phi \leq 25$	all ϕ	$25 < \phi < 165$	———
Left Horizontal Stabilizer	$90 \leq \phi \leq 225$	all ϕ	$225 < \phi < 90$	———
Right Horizontal Stabilizer	$135 \leq \phi \leq 270$	all ϕ	$270 < \phi < 135$	———
Left Wing Pod	$-25 \leq \phi \leq 200$	all ϕ	$200 < \phi < -25$	———
Right Wing Pod	$160 \leq \phi \leq 25$	all ϕ	$25 < \phi < 160$	———

Component		Visible Region		Shadow Region	
Fuselage		all (θ,ϕ)		———	
Vertical Stabilizer		$0 \leq \theta \leq 90$ all ϕ	$90 < \theta < 180$ $130 \leq \phi \leq 230$	$0 \leq \theta \leq 90$ ———	$90 < \theta < 180$ $230 < \phi < 130$
Left Engine Intake	Duct	$0 \leq \phi \leq 25$ and $\lvert\theta - 90\rvert \leq 25$		otherwise	
	Termination	$0 \leq \phi \leq 20$ and $\lvert\theta - 90\rvert \leq 20$		otherwise	
Right Engine Intake	Duct	$-25 \leq \phi \leq 0$ and $\lvert\theta - 90\rvert \leq 25$		otherwise	
	Termination	$-20 \leq \phi \leq 0$ and $\lvert\theta - 90\rvert \leq 20$		otherwise	
Engine Exhaust	Duct	$\lvert\phi\rvert \leq 60$ and $\lvert\theta - 90\rvert \leq 60$		otherwise	
	Termination	$\lvert\phi\rvert < 60$ and $\lvert\theta - 90\rvert \leq 60$		otherwise	

1) Select aspect angles θ and ϕ in the TCS, and an incident field in the form of Equation (3.1).

2) Transform θ and ϕ to local aspect angles $\theta^{(n)}$ and $\phi^{(n)}$, using Equations (4.4) and (4.5).

3) Transform incident field to local coordinates using Equation (4.9).

4) Compute backscattered field using one of the equations in Chapter 3.

5) Take into consideration the shadowing effect, and multiply the amplitude of the scattered field by a proper modulation function using Equation (4.17).

6) Transform the backscattered field to the TCS using Equation (4.13).

7) Repeat steps 2) through 6) for all components.

8) Compute total scattered field in TCS by using

$$\underline{\underline{E}}^{(BS)} = \sum_{A=1}^{N} \underline{\underline{E}}^{(BS),(n)} \cdot \exp[i\phi^{(n)}]$$

where $\phi^{(n)}$ is the phase shift in Equation (4.16).

9) Compute scattering parameters using Equations (2.8) and (2.9).

4.4 Digital Computer Modeling of Surfaces

From the above discussion, it is clear that the two key steps in using the present ray-optics approach are (i) locating of scattering centers, and (ii) determining which, if any, of the scattering centers are shadowed by other components of the target. For simple geometrical bodies, such as an ellipsoid, plate, cylinder, etc., this task is not too difficult. For more complex geometrical bodies that may be considered later, it does not seem to be analytically manageable. In the past contract period, we have investigated a computer-aided modeling technique, which promises to generate arbitrary surfaces and determine scattering centers and shadowing effects in an automatic fashion. Some of the preliminary results are given below.

A. General Approach to Modeling a Three-Space Surface

Two basic methods exist for digital computer modeling of surfaces. The surface may be represented by some analytical function describing the entire locus, or it may be represented by a data set describing individually sampled points on the surface. In the course of several years of research into digital display of three-dimensional solids, the latter method has been chosen as the more flexible and efficient.

The general modeling techniques employed in this work approximate a three-space surface by a data set consisting of an ensemble of planar polygons whose vertices lie on the surface of interest. These polygons may have any number of vertices but must, however, be convex. For this reason triangles or quadrilaterals are most commonly used.

Each polygon is represented by a data set which includes the triplets of the vertices, a reflectivity coefficient, and the three coefficients of the general form of the plane in which the polygon lies. These three coefficients are equivalent to the magnitudes of the components of a unit vector normal to the polygon.

Once a surface has been modeled by a set of polygonal systems, programs are available to display the surface in a variety of modes. The simplest form of display consists of a "wire frame" or line drawing of the surface. The surface is represented by displaying lines along all the edges of the polygons in Figure (4.4). Algorithms are also available for producing a grey-scale solid rendering of the surface with all hidden lines and planes removed [Figure (4.5)]. These algorithms determine all plane intersections, all hidden or shadowed planes, and the radiant flux falling on each plane because of a movable radiation source.

These algorithms essentially model the optical properties of the surface in question and then perform a perspective transformation for display purposes.

Several methods are available for constructing the polygonal data set. Measurements may be taken directly from the surface to be modeled, or data points may be generated from an analytical expression for the surface.

B. Polygonal Modeling of a Surface Described by a Function of Two Variables

A software surface modeling system has been developed for operation on the CDC 1604 computing system of the Coordinated Science Laboratory (CSL), University of Illinois. Parts of this system will assemble a polygonal data set from arrays of computed triplets lying on a given locus. The triplets are computed from the analytical expression of the surface in question. The values are packed in three two-dimensional arrays; for X, Y, and Z. The points are related positionally. Each possible set of four adjacent points is examined to generate plane data; the (i,j), (i + 1,j), (i,j + 1), and the (i + 1,j + 1) elements of the array. For every four-point set, two pairs of triangular planes are possible. That pairing is chosen which produces the smaller dihedral angle between planes. This gives the smoothest approximation to the surface.

The system then computes the normal coefficients and the user may supply a reflectivity coefficient. The data set is written on magnetic tape in a format compatible with the display algorithms. This data set may be inputted to the display systems or used for further calculations.

This method gives a very good approximation to the surface. However, a few precautions are necessary. First, the function must be adequately sampled. Sampling frequency is determined by resolution requirements. The finer the sampling, the better the fit of the polygon function to the surface. Second, the sampling should be finer at points of greatest curvature. The polygons should not be of equal area, rather the difference in normal vector orientation between two polygons should be constant, that is, the angle between any two polygons should be the same.

For many functions it is difficult if not impossible to analytically derive expressions for curvature. Even when possible, this technique may not be desirable because of excessive computation time. A general procedure for sampling a function so as to produce a polygonal model reasonably sensitive to changes in curvature is to simply sample the function in a regular rectangular grid in the x, y plane. This has the effect of

producing larger planes as the angle between the x, y plane and the tangent plane increases. This makes the polygon area approximately proportional to the radius of curvature in the region of the polygon.

A computer program has been developed to simulate aircraft surfaces by an arbitrary number of ellipsoidal surfaces. Each ellipsoid is specified by some function $z = f(x,y)$. The coordinate system is centered on the aircraft model. It is assumed that the function contains terms for rotation and translation which position the ellipsoids correctly with respect to each other. The program developed has been used for extensive modeling of an aircraft composed of 8 ellipsoids. The results are shown in Figures (4.6) and (4.7).

Figure 4.4. A "wire frame" display of an ellipsoid

Figure 4.5. A polygonal model display of an ellipsoid

Figure 4.6. An aircraft modeled by using six ellipsoids (top view)

Figure 4.7. An aircraft modeled by using eight ellipsoids (top view)

5. NUMERICAL RESULTS

The numerical computations have been made for the two aircraft: T-33, and BQM-34A. In each case, the RCS, azimuth error, and elevation error are calculated as a function of the azimuth angle ϕ at an increment of 1 degree, while other parameters such as elevation angle θ, frequency, and polarization are fixed.

5.1 T-33 Aircraft

In reference [33], the RCS of a one-half scale T-33 model was measured by a nanosecond short-pulse radar. Its data provide a check for the present computer program. In Figures 5.2 and 5.3, the experimental data and the theoretical prediction are presented when the frequencies are 8.8 GHz and 2.9 GHz, respectively, with vertical polarization ($E_\theta = 0$) and $\theta = \pi/2$.

It should be noted that the data given in reference [33] were measured from a half-scaled model, while the results presented in Figures 5.2 and 5.3 have been increased 6 db to compensate for the scale factor. The agreement between the experimental and the theoretical results is reasonably good except in the neighborhood of $\phi = 0^\circ$ (head-on),

and $\phi = 180^{\circ}$ (tail-on). In the head-on, or tail-on directions, the main contribution to the scattering comes from the engine duct. The fact that good agreement is not obtained in these two directions indicates the need of an improved model for the engine duct. This task will be carried out in the next contract period.

In addition to the case $\theta = 90^{\circ}$ as discussed above, the experimental data for the T-33 are also available when the aircraft is tilted at an angle Ψ from the horizontal plane (Figure 5.1). The corresponding aspect angles (θ,ϕ) due to such a tilt can be found from the transformation in Equation (4.1) with $\beta = -\Psi$, $\alpha = 0$, and $\gamma = 0$. For the frequency 8.8 GHz with $\Psi = 5^{\circ}$, and for the frequency 2.9 GHz with $\Psi = 5^{\circ}$ and $\Psi = 10^{\circ}$, the experimental and the theoretical calculations are presented in Figures 5.4, 5.6, and 5.7 respectively. The agreement is reasonably good, but not as good as that presented in Figures 5.2 and 5.3. This is due to the facts that the experimental model of the T-33 is more complex in structure than the model described in Table 2.2, and that the difference in structures becomes more predominant when the aspect angle θ is different from $\pi/2$. The accuracy can be improved if more components are

used in Table 2.2. However, this can be achieved only at the expense of computational labor.

5.2 BQM-34A Target Drone

This aircraft was also studied by Wright who used ellipsoids to approximate the various components of the aircraft. In Figures 5.7, 5.8, and 5.9, we present a comparison between his results and ours for the RCS, e_θ, and e_ϕ as functions of the azimuthal angle ϕ at frequency 1 GHz, with vertical polarization incidence ($E_\theta = 0$), and $\theta = \pi/2$. The agreement is good except in the neighborhood of head-on and tail-on directions, because the scattering from the duct is taken into consideration in our computation (See Sections 3.3 and 3.4), while it is not included in Wright's computation.

To study the frequency dependence of the scattering parameters, more computations were made by changing the frequency from 1 GHz (Figures 5.10, 5.11, and 5.12) to 5 GHz (Figures 5.13, 5.14, and 5.15), and to 8 GHz (Figures 5.16, 5.17, and 5.18), while the other parameters are kept the same as the ones used in Figures 5.7, 5.8, and 5.9. As may be expected, the RCS is not frequency-sensitive in the broadside

direction. In that direction, the main contribution to the scattering comes from the fuselage, which is modeled by an ellipsoid in the present study. As given in Equation (3.4), the backscattering from an ellipsoid is independent of frequency.

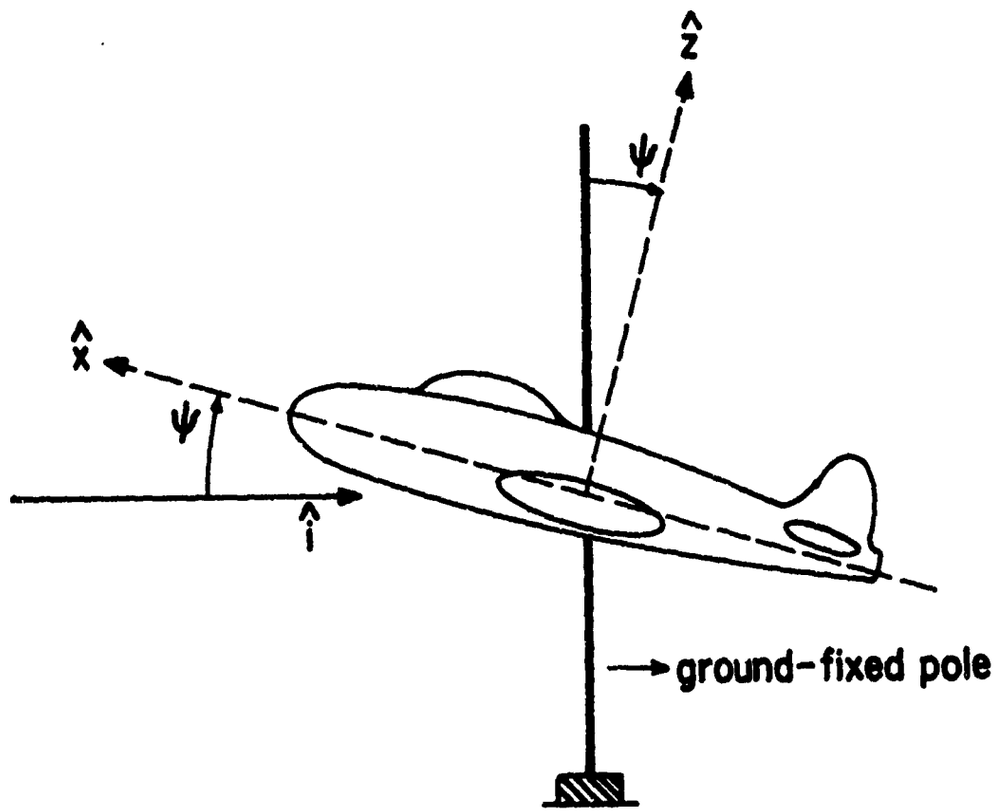

Figure 5.1. T-33 tilt angle rotation convention

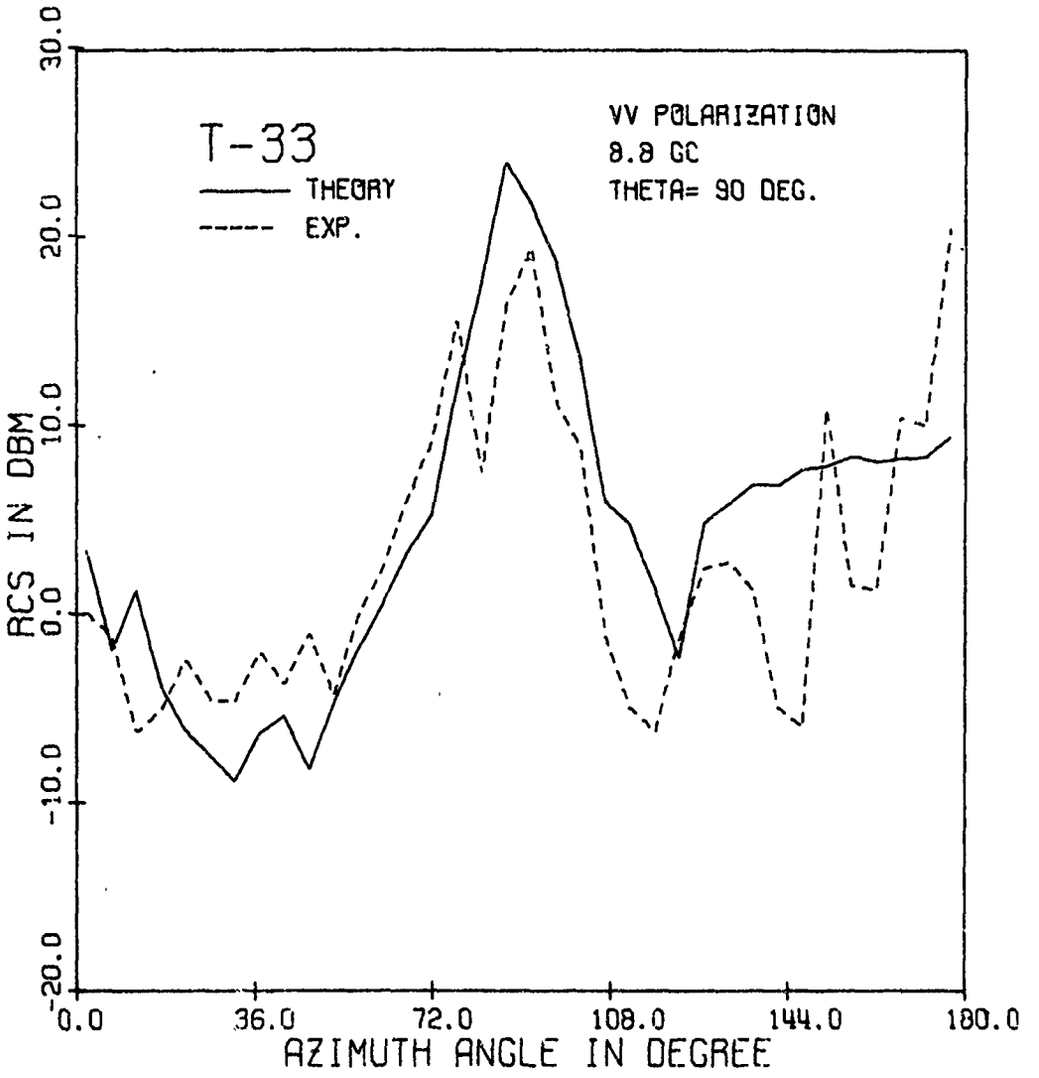

Figure 5.2. RCS in db per square meter of a full-scaled T-33 aircraft as a function of azimuth angle ϕ for a fixed $\theta = 90^{\circ}$, for a vertically polarized incident plane wave ($E_{\theta} = 0$), and at frequency 8.8 GHz. The solid line represents the 5°-average of the theoretical computation. The dotted line represents the 5°-median of the experiment reported in reference [33].

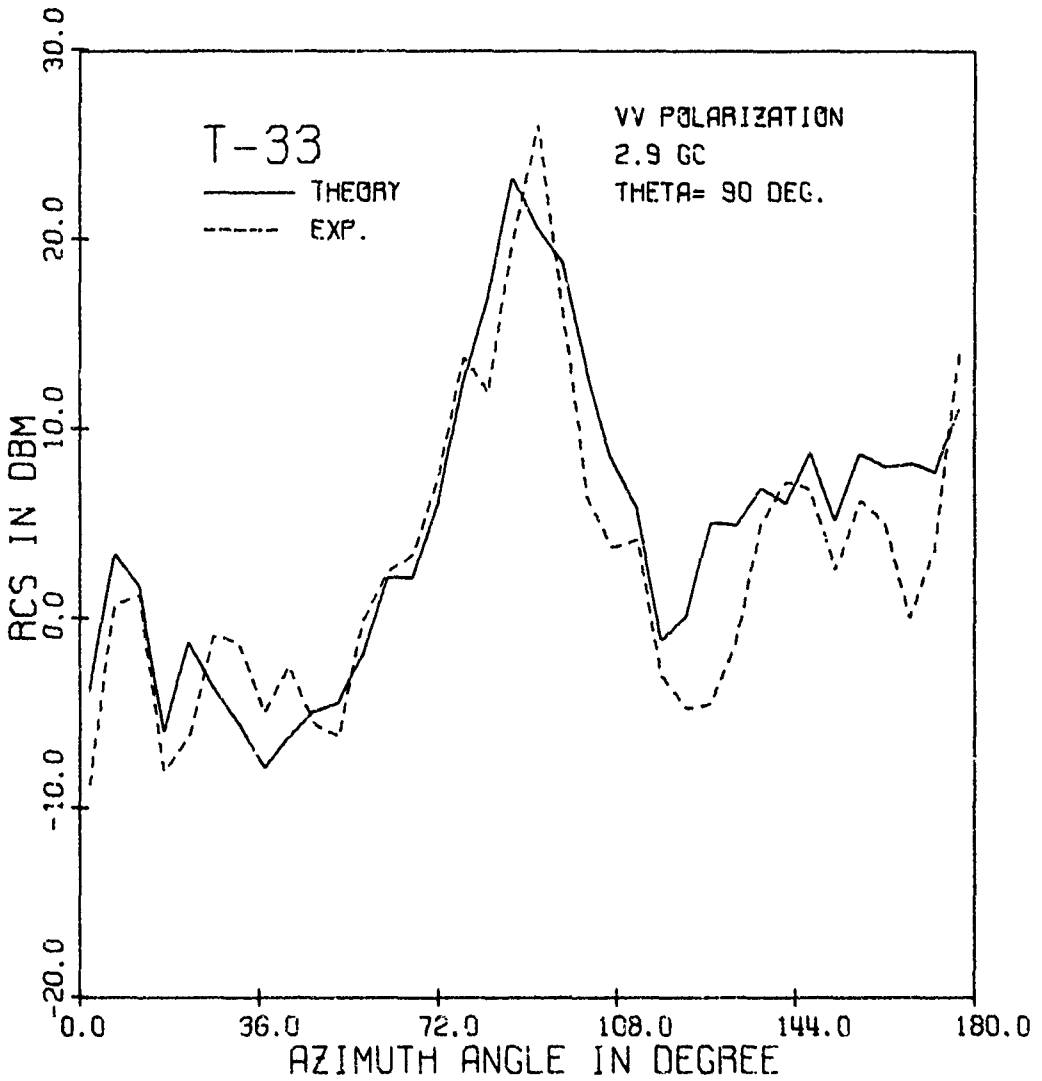

Figure 5.3. RCS in db per square meter of a full-scaled T-33 aircraft as a function of azimuth angle ϕ for a fixed $\theta = 90^{o}$, for a vertically polarized incident plane wave ($E_{\theta} = 0$), and at frequency 2.9 GHz. The solid line represents the 5^{o}-average of the theoretical computation. The dotted line represents the 5^{o}-median of the experiment reported in reference [33].

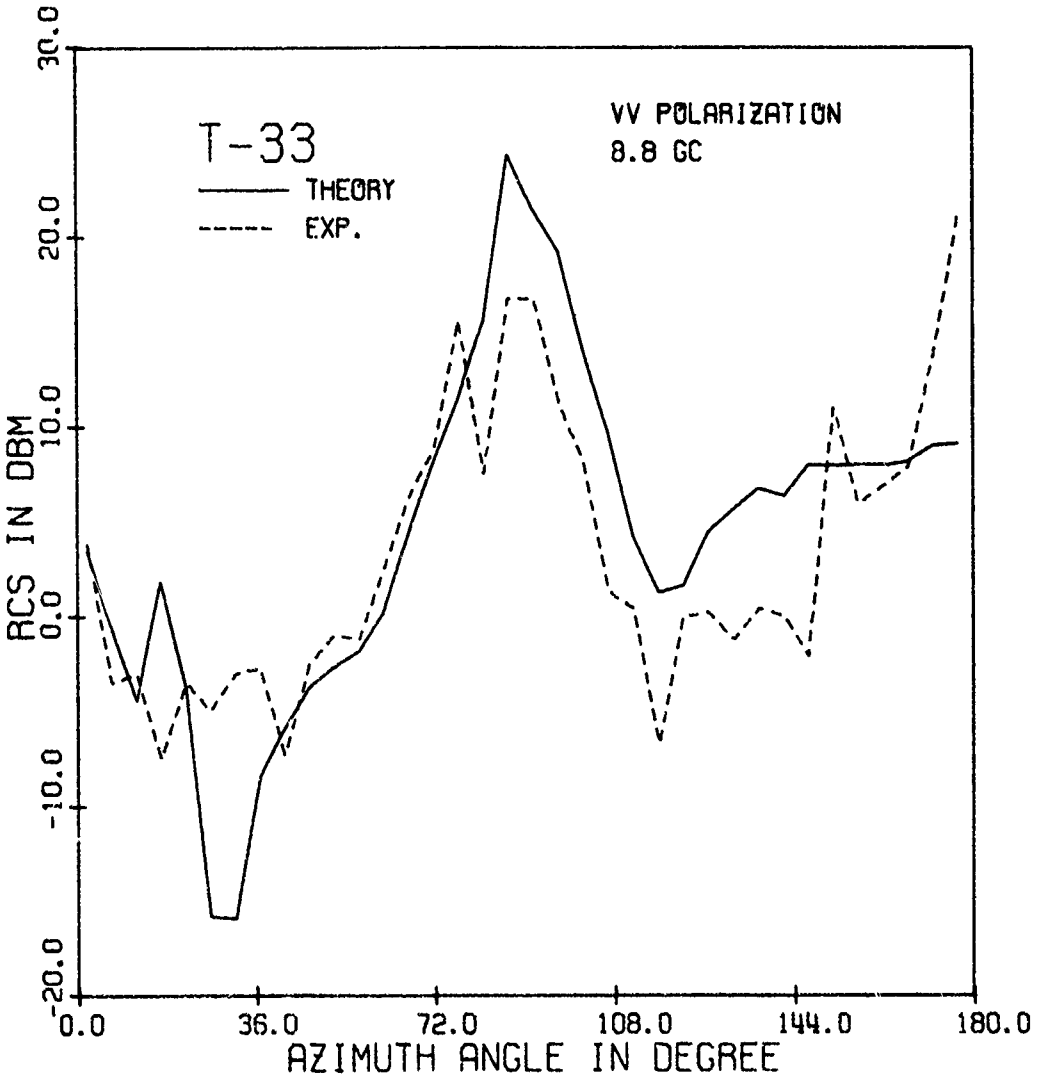

Figure 5.4. RCS in db per square meter of a full-scaled T-33 aircraft as a function of azimuth angle ϕ for a tilt angle $\Psi = 5^{o}$, for a vertically polarized incident plane wave ($E_{\theta} = 0$), and at frequency 8.8 GHz. The solid line represents the 5^{o}-average of the theoretical computation. The dotted line represents the 5^{o}-median of the experiment reported in reference [33].

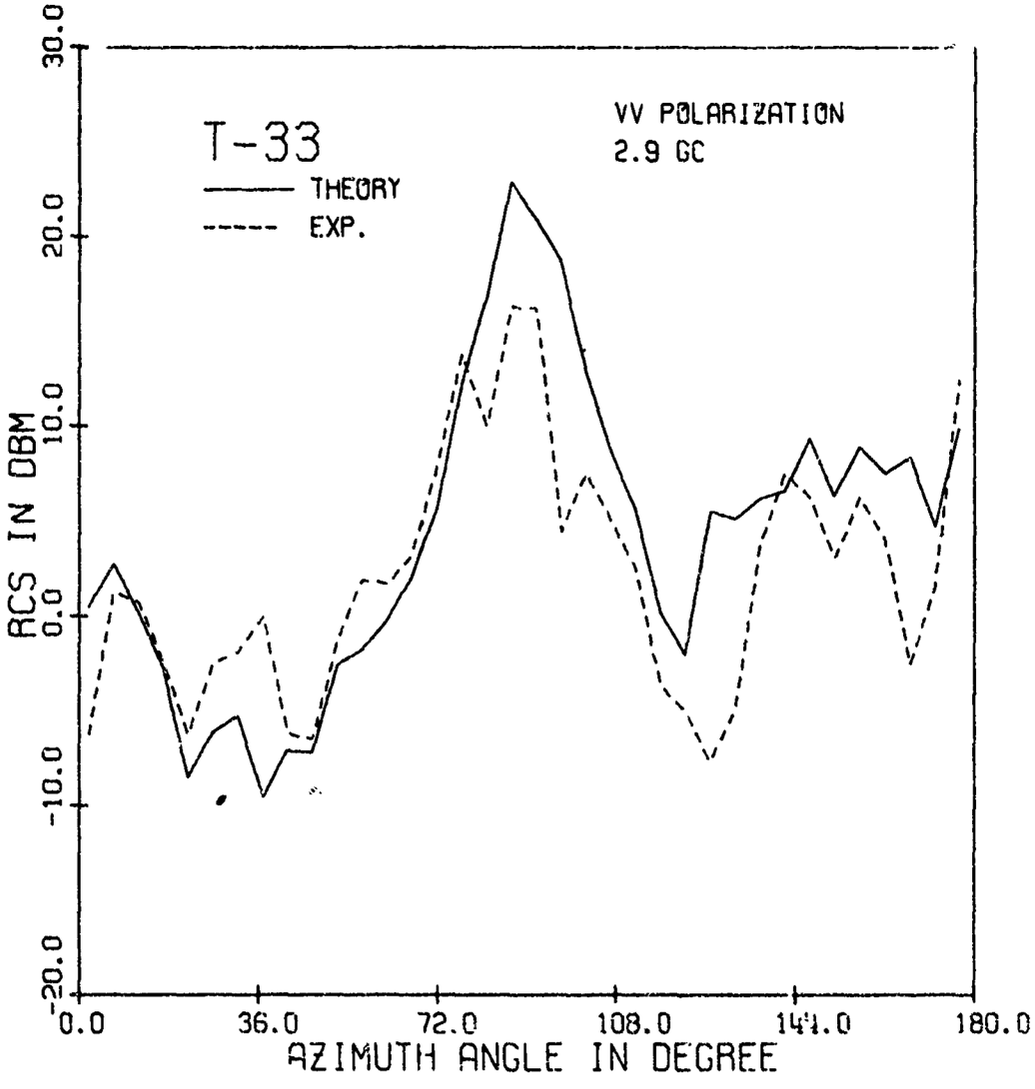

Figure 5.5. RCS in db per square meter of a full-scaled T-33 aircraft as a function of azimuth angle ϕ for a tilt angle $\Psi = 5^{o}$, for a vertically polarized incident plane wave ($E_{\theta} = 0$), and at frequency 2.9 GHz. The solid line represents the 5^{o}-average of the theoretical computation. The dotted line represents the 5^{o}-median of the experiment reported in reference [33].

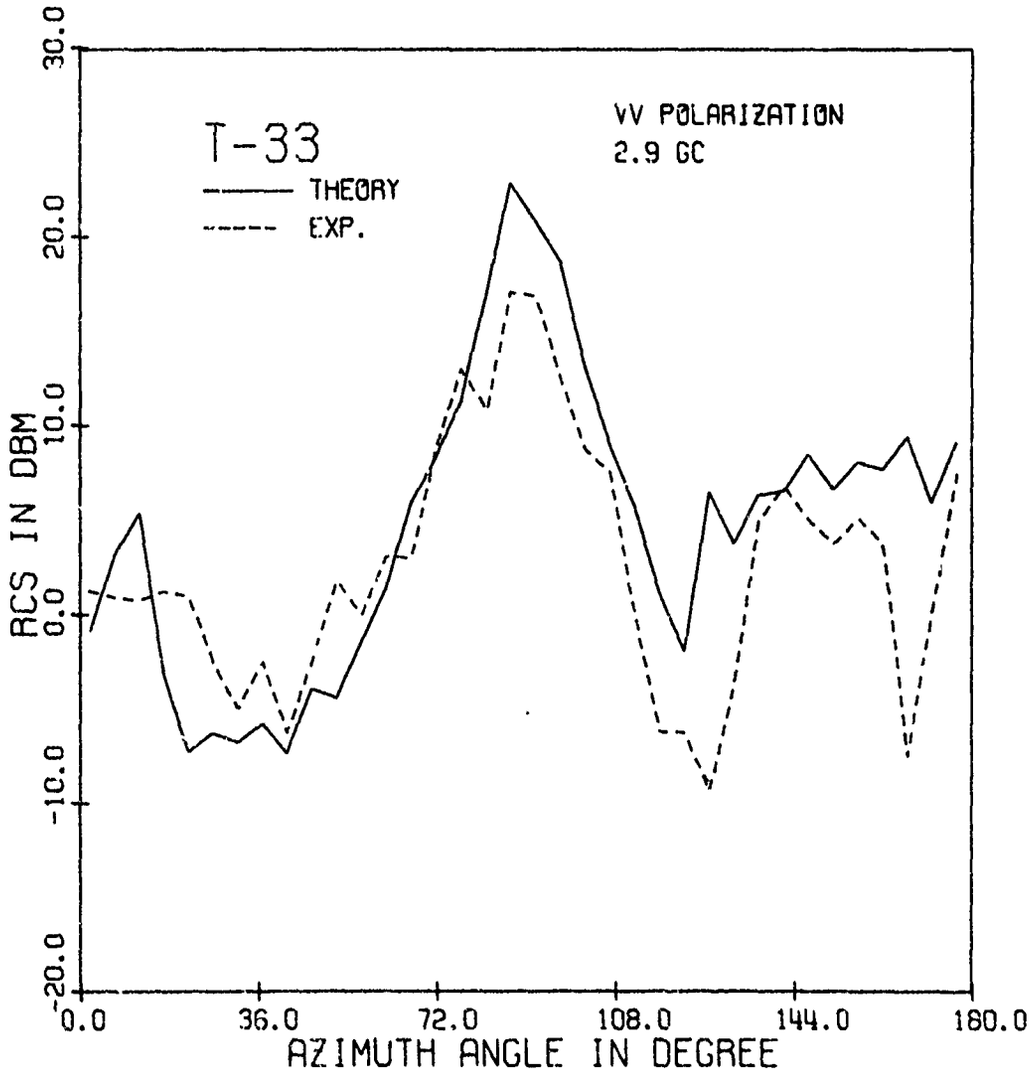

Figure 5.6. RCS in db per square meter of a full-scaled T-33 aircraft as a function of azimuth angle ϕ for a tilt angle $\Psi = 10^{o}$, for a vertically polarized incident plane wave ($E_{\theta} = 0$), and at frequency 2.9 GHz. The solid line represents the 5^{o}-average of the theoretical computation. The dotted line represents the 5^{o}-median of the experiment reported in reference [33].

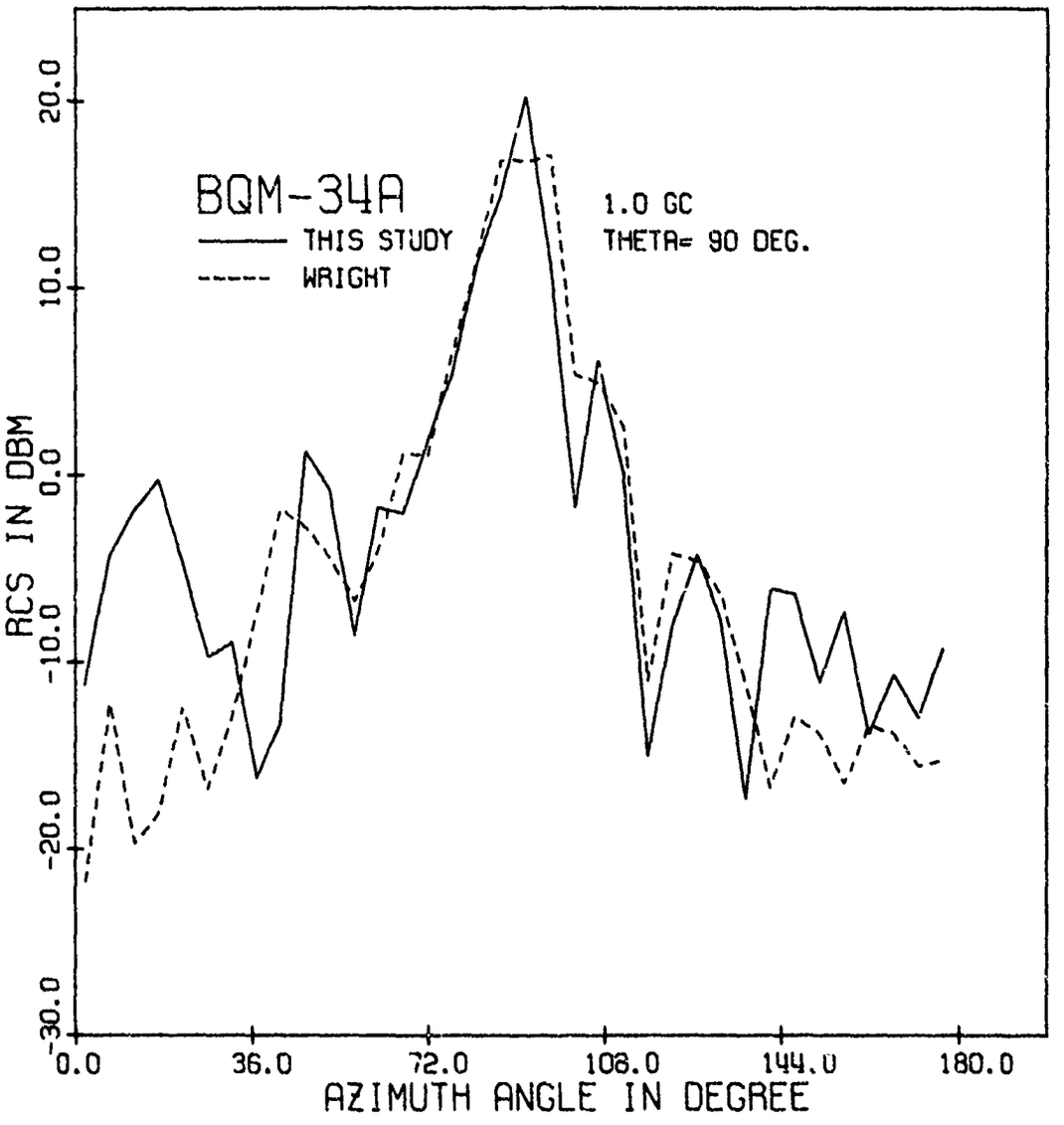

Figure 5.7. RCS in db per square meter of the BQM-34A drone as a function of azimuth angle ϕ for a fixed $\theta = 90^{o}$, for a vertically polarized incident plane wave ($E_{\theta} = 0$), and at frequency 1 GHz. The solid line represents the 5^{o}-median computation of our model. The dotted line represents the 5^{o}-median computation of Wright's model using ellipsoids.

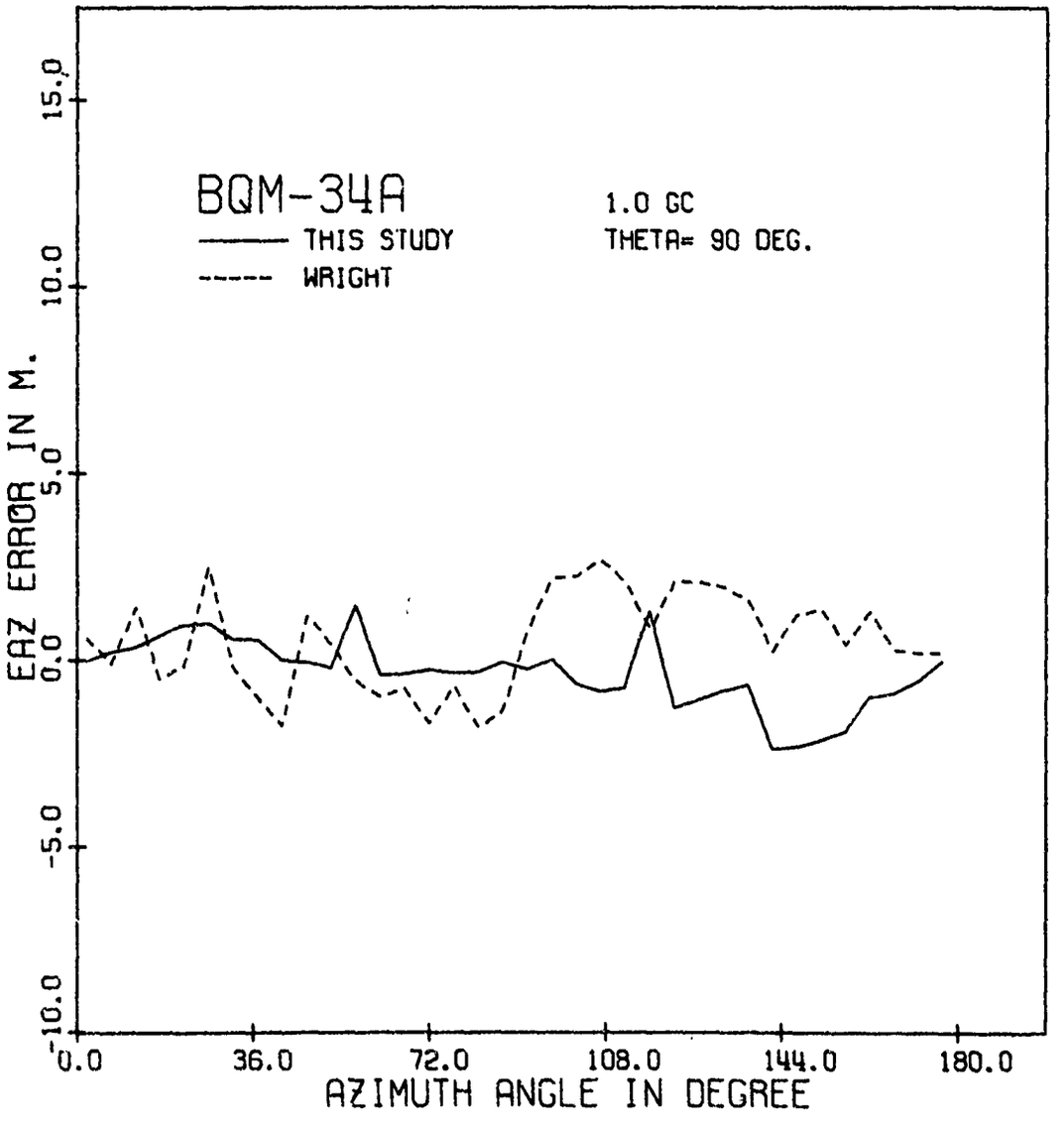

Figure 5.8. Azimuth error (e_ϕ) in meters of the BQM-34A drone as a function of azimuth angle ϕ for a fixed $\theta = 90^o$, for a vertically polarized incident plane wave ($E_\theta = 0$), and at frequency 1 GHz. The solid line represents the 5^o-median computation of our model. The dotted line represents the 5^o-median computation of Wright's model using ellipsoids.

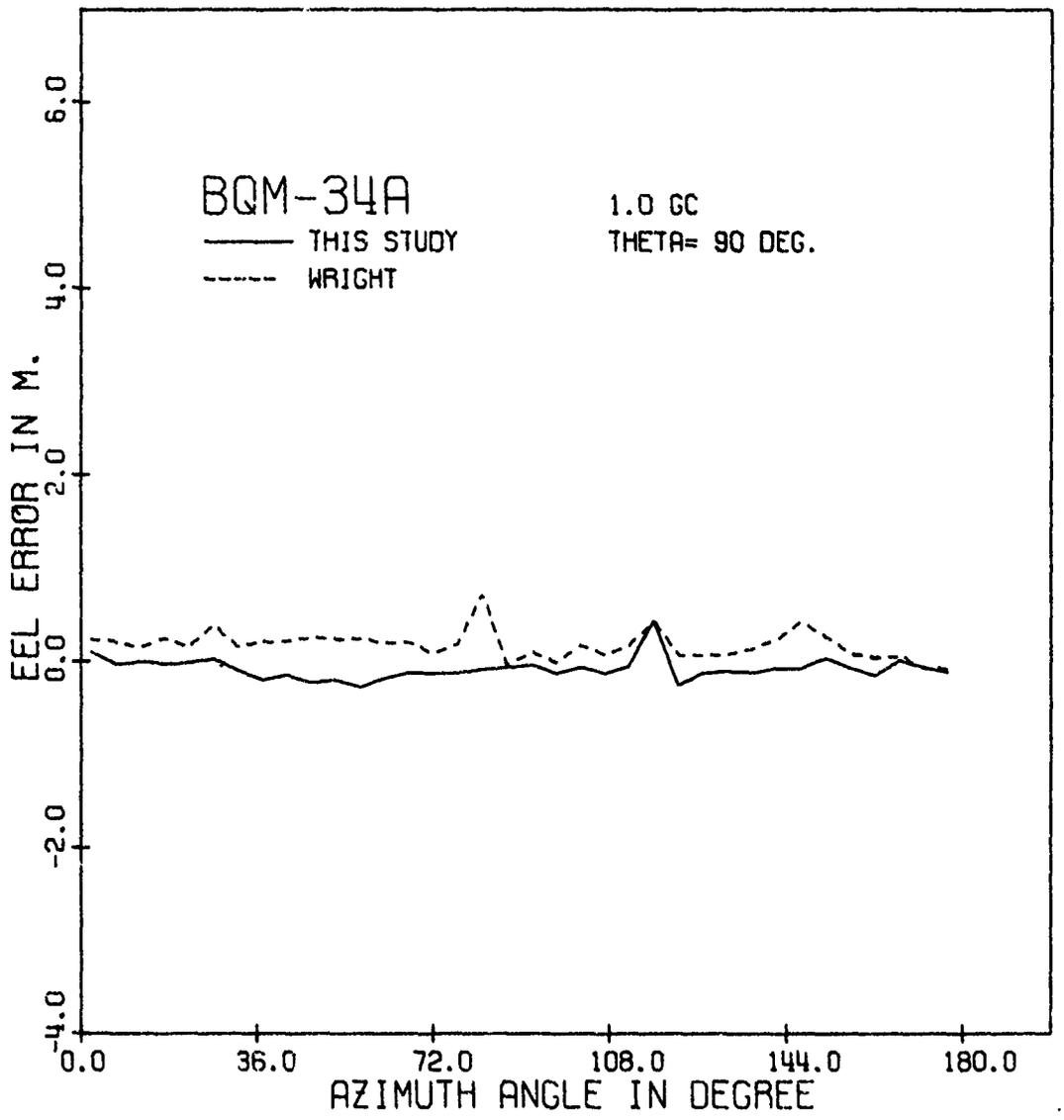

Figure 5.9. Elevation error (e_θ) in meters of the BQM-34A drone as a function of azimuth angle ϕ for a fixed $\theta = 90^\circ$, for a vertically polarized incident plane wave ($E_\theta = 0$), and at frequency 1 GHz. The solid line represents the 5°-median computation of our model. The dotted line represents the 5°-median computation of Wright's model using ellipsoids.

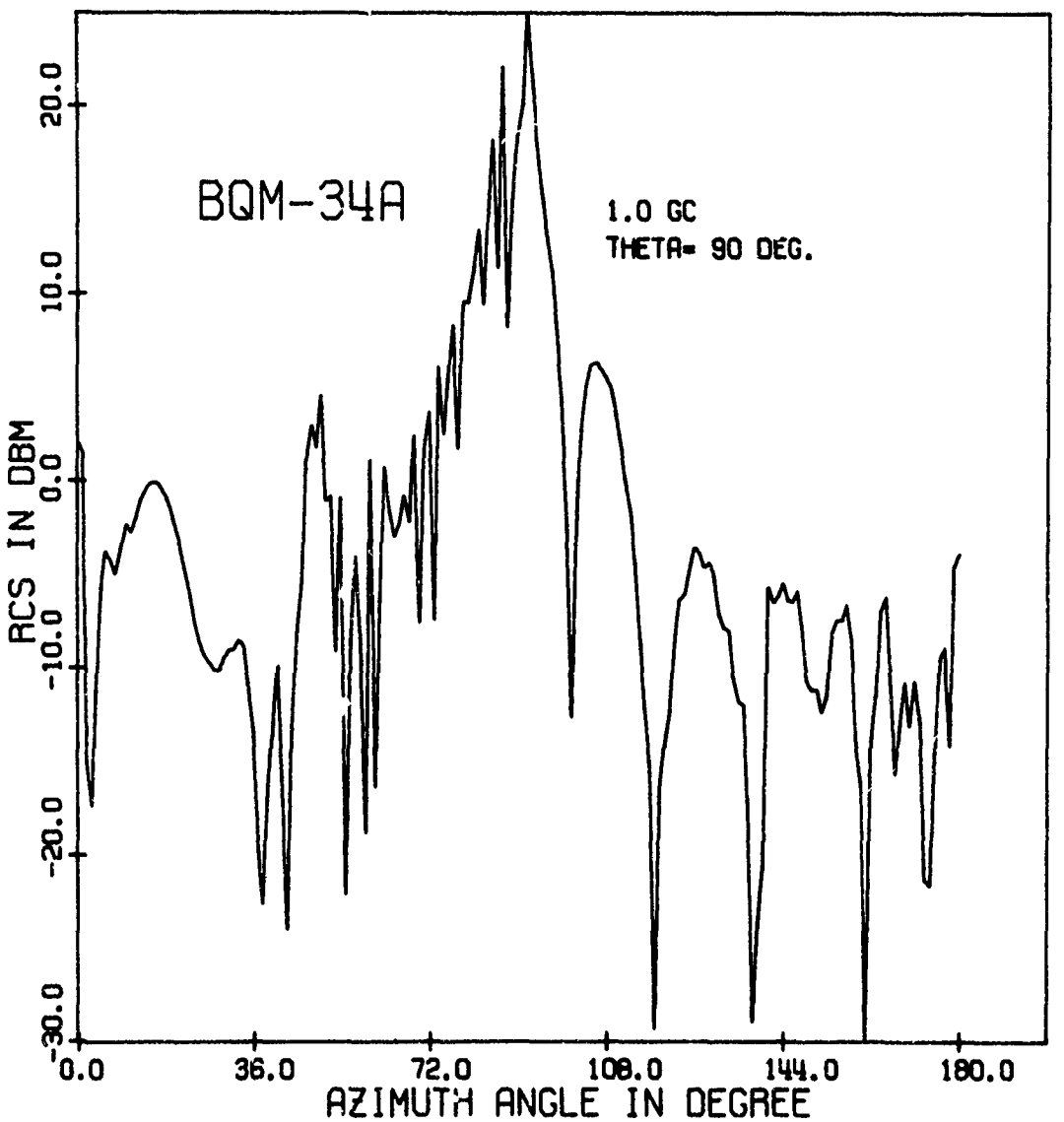

Figure 5.10. RCS in db per square meter of the BQM-34A drone as a function of azimuth angle ϕ for a fixed $\theta = 90^{o}$, for a vertically polarized incident plane wave ($E_{\theta} = 0$), and at frequency 1 GHz

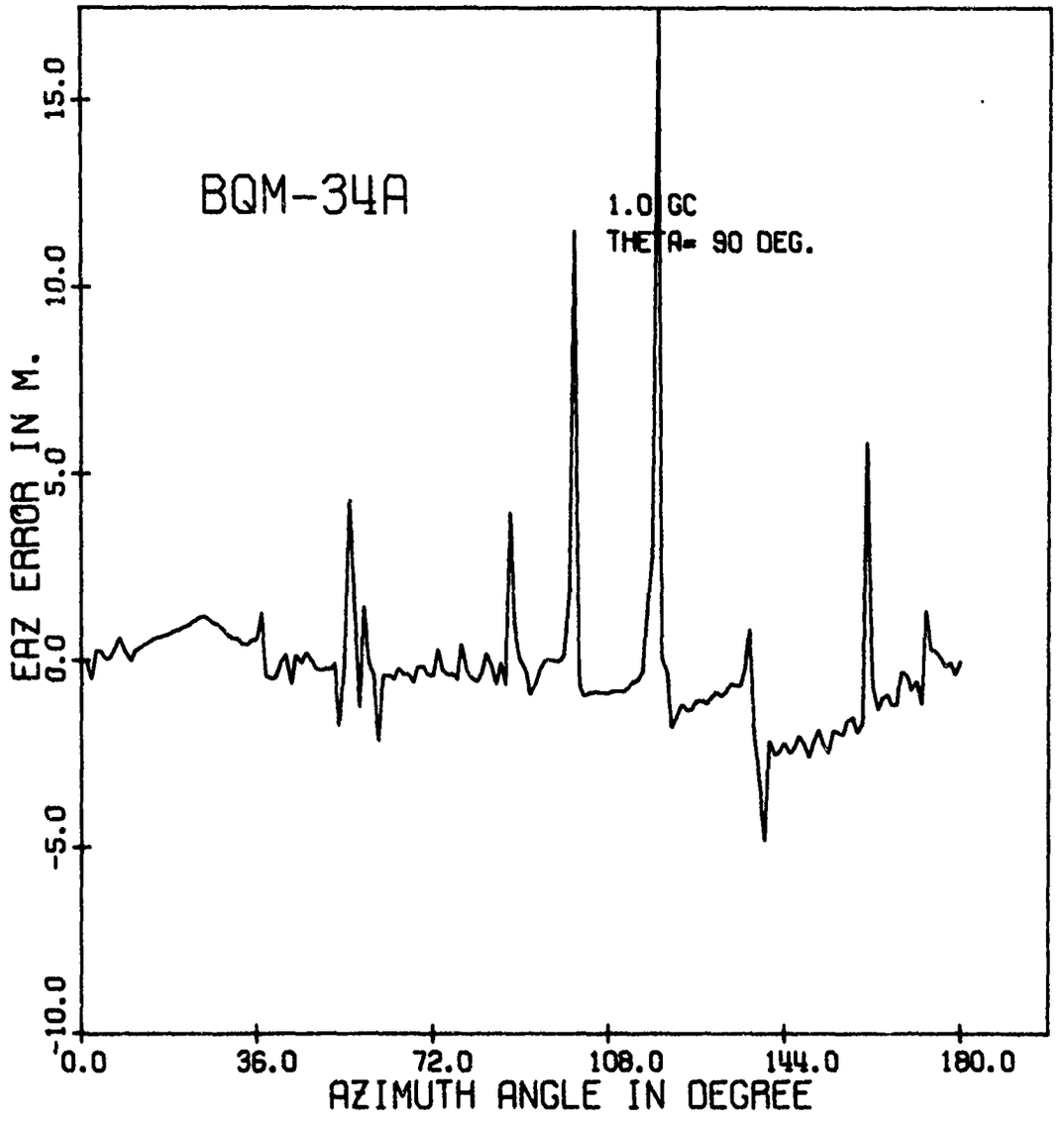

Figure 5.11. Azimuth error (e_ϕ) in meters of the BQM-34A drone as a function of azimuth angle ϕ for a fixed $\theta = 90^o$, for a vertically polarized incident plane wave ($E_\theta = 0$), and at frequency 1 GHz

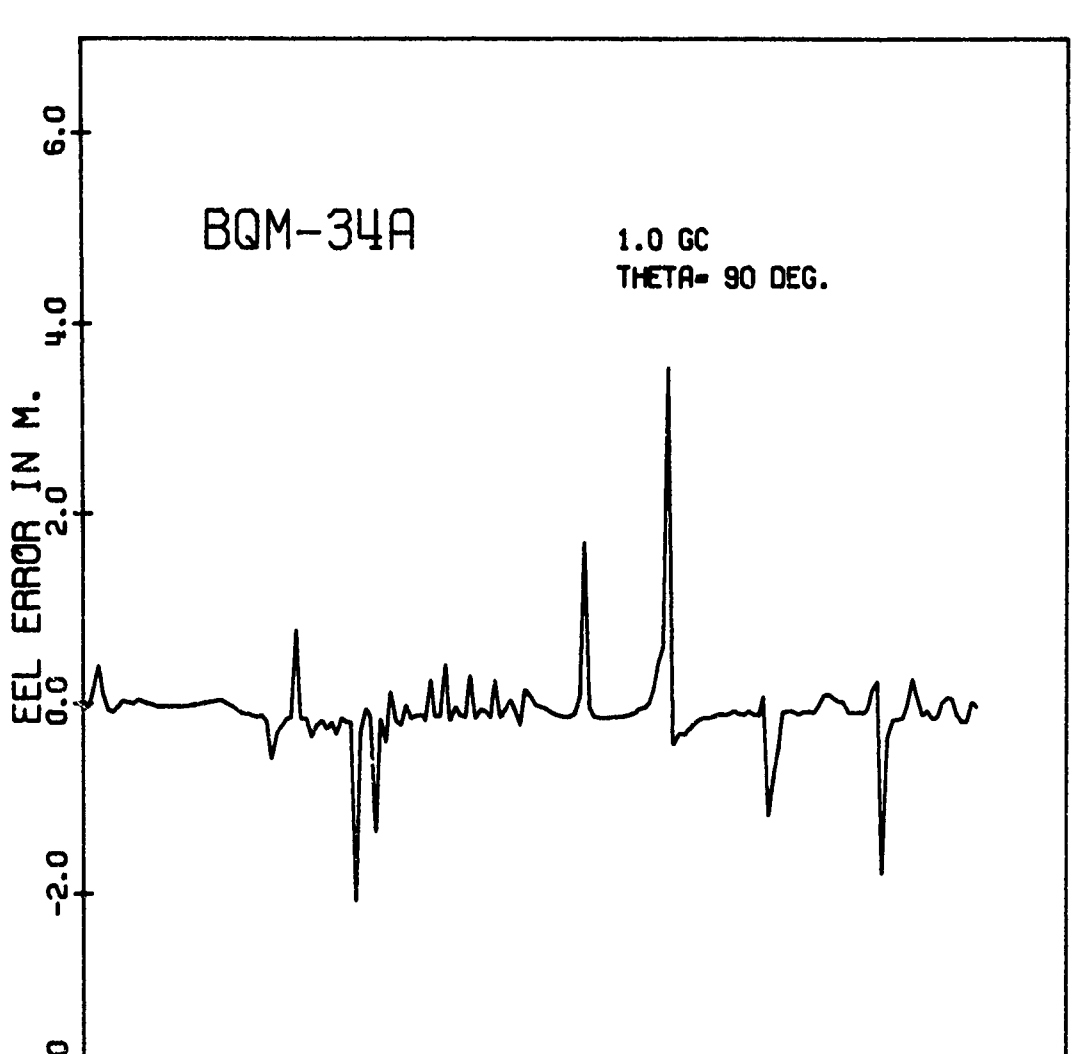

Figure 5.12. Elevation error (e_θ) in meters of the BQM-34A drone as a function of azimuth angle ϕ for a fixed $\theta = 90^o$, for a vertically polarized incident plane wave ($E_\theta = 0$), and at frequency 1 GHz

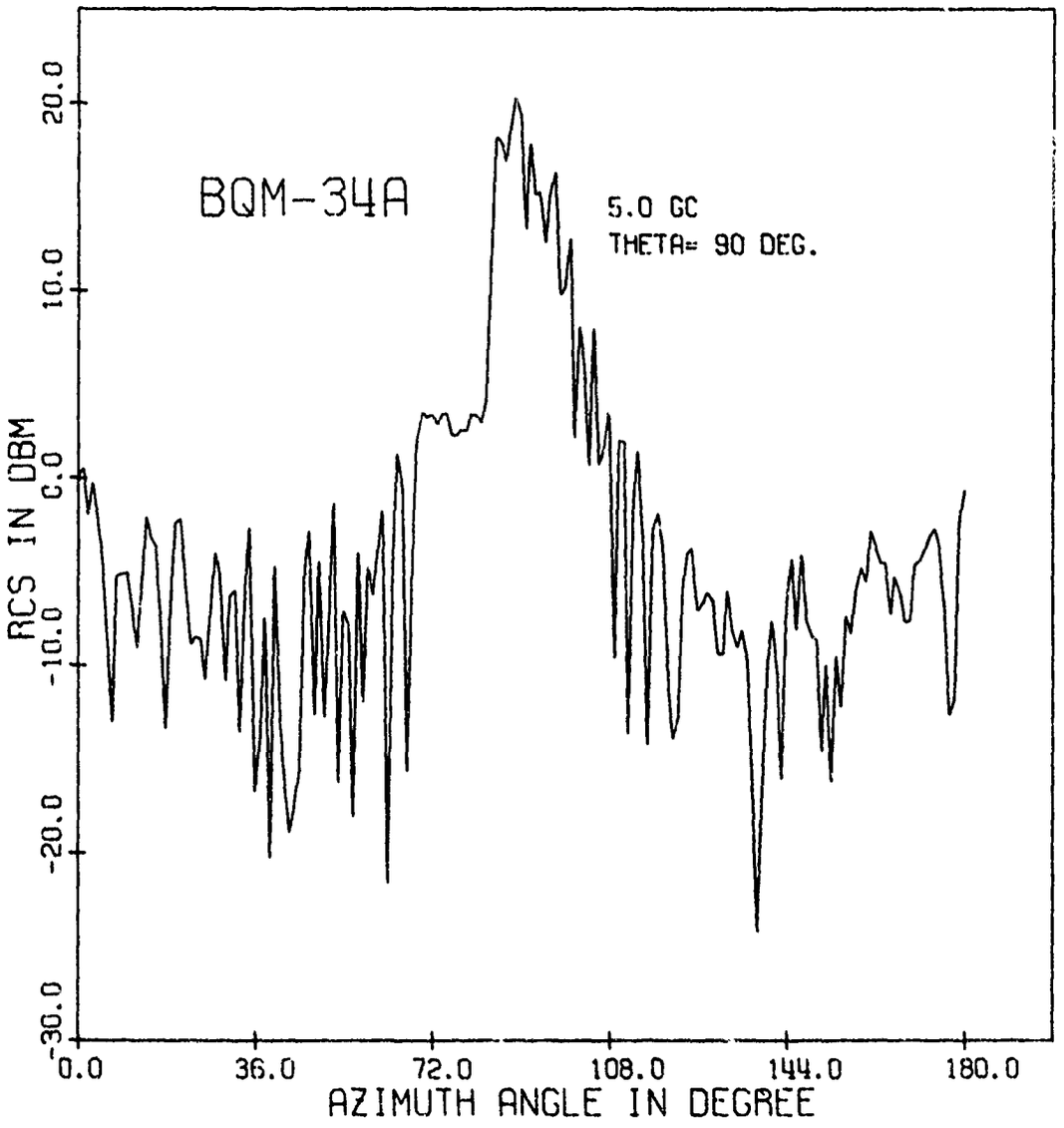

Figure 5.13. RCS in db per square meters of the BQM-34A drone as a function of azimuth angle ϕ and a fixed $\theta = 90^{o}$, for a vertically polarized incident plane wave ($E_{\theta} = 0$), and at frequency 5 GHz

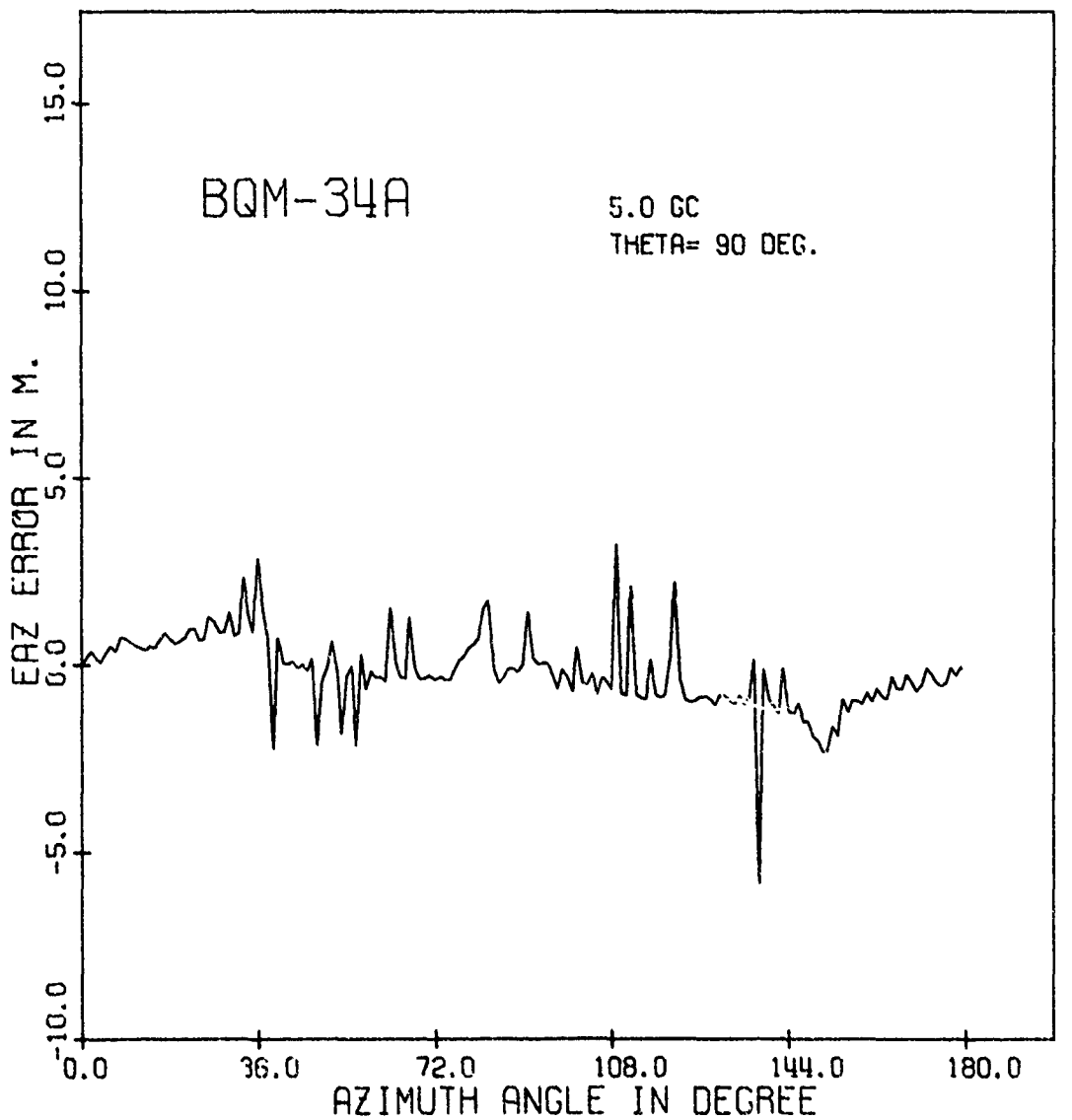

Figure 5.14. Azimuth error (e_ϕ) in meters of the BQM-34A drone as a function of azimuth angle ϕ for a fixed $\theta = 90^\circ$, for a vertically polarized incident plane wave ($E_\theta = 0$), and at frequency 5 GHz

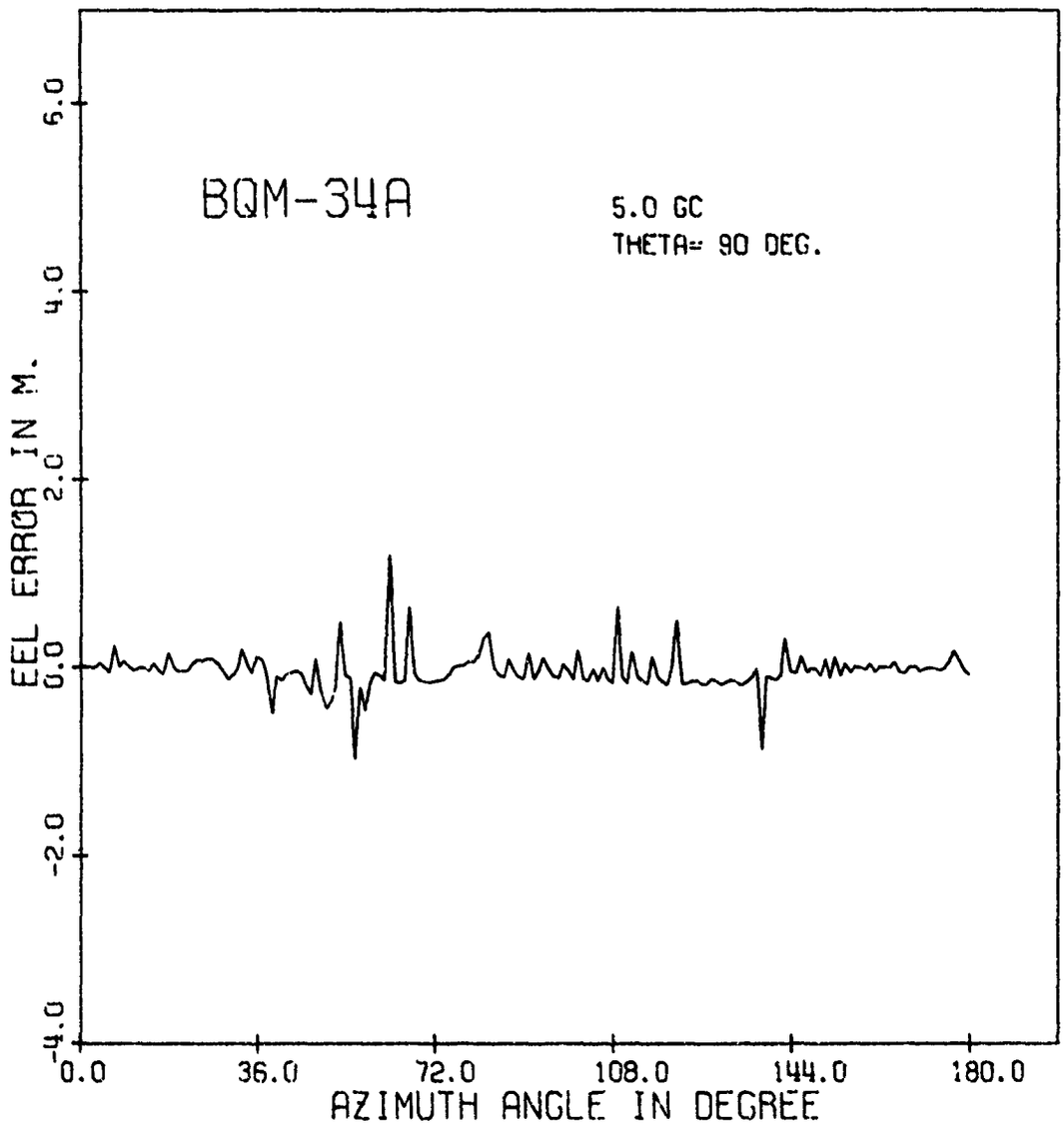

Figure 5.15. Elevation error (e_θ) in meters of the BQM-34A drone as a function of azimuth angle ϕ and a fixed $\theta = 90^\circ$, for a vertically polarized incident plane wave ($E_\theta = 0$), and at frequency 5 GHz

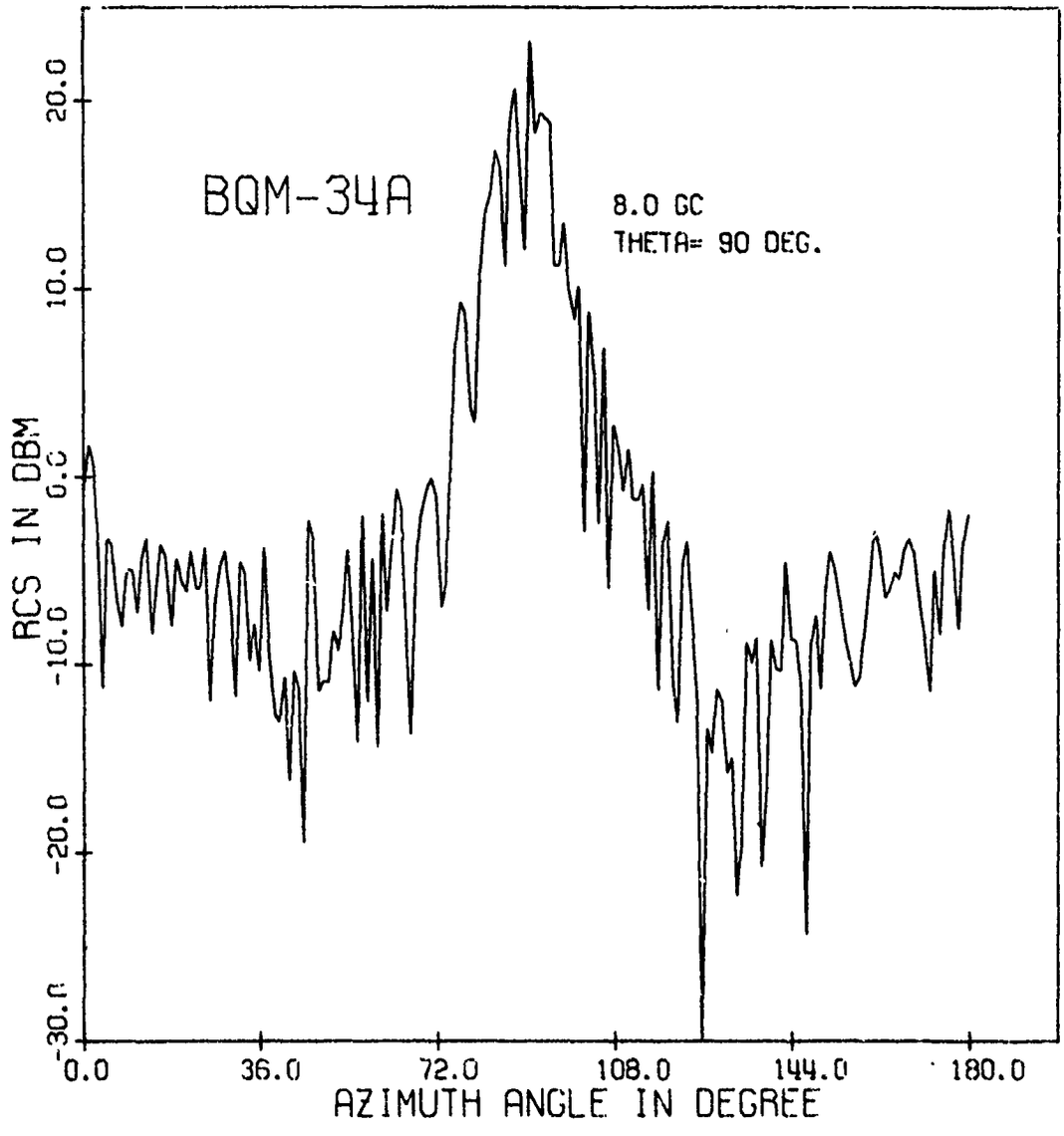

Figure 5.16. RCS in db per square meters of the BQM-34A drone as a function of azimuth angle ϕ and a fixed $\theta = 90^{o}$, for a vertically polarized incident plane wave ($E_{\theta} = 0$), and at frequency 8 GHz

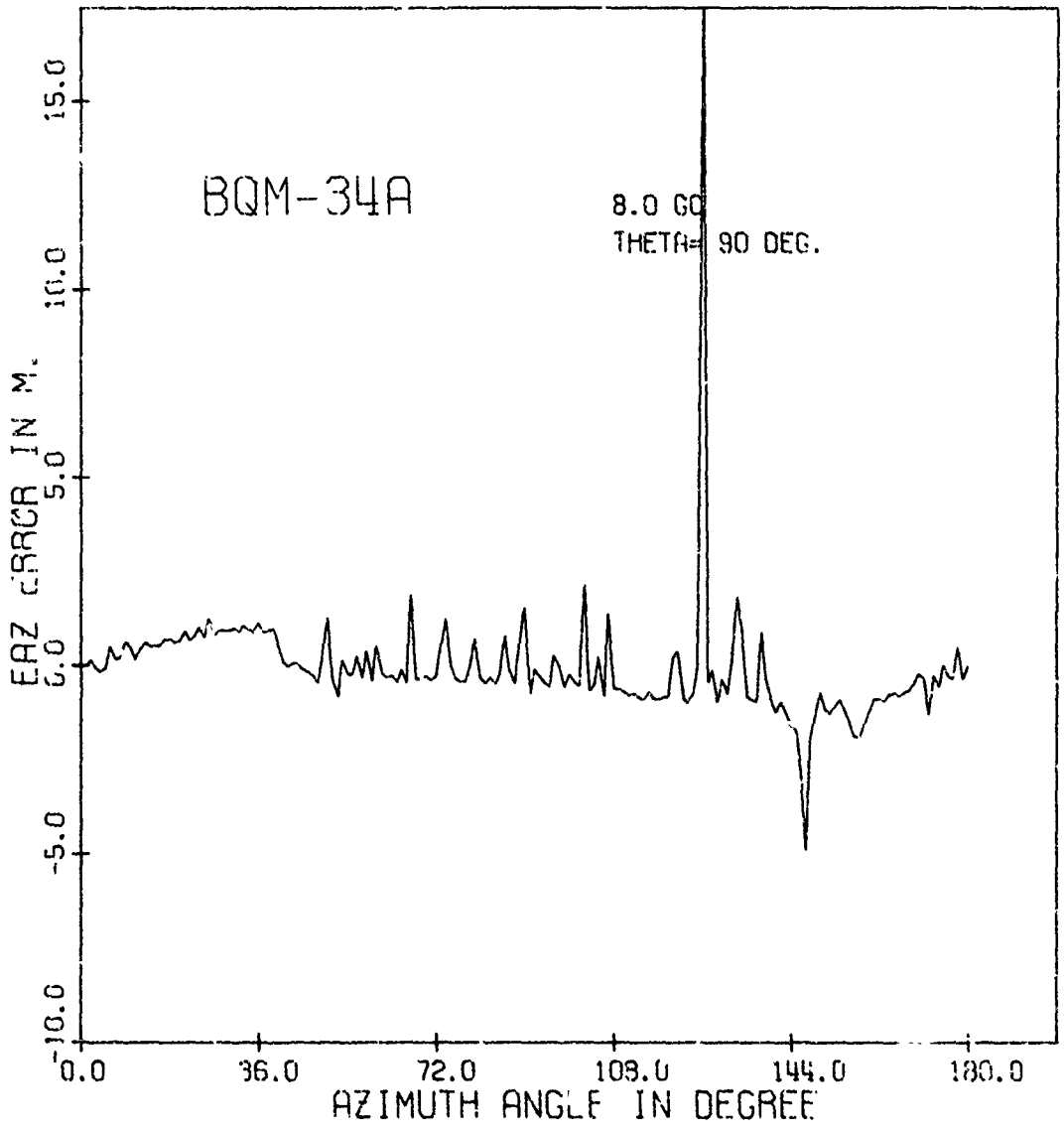

Figure 5.17. Azimuth error (e_ϕ) in meters of the BQM-34A drone as a function of azimuth angle ϕ for a fixed $\theta = 90^\circ$, for a vertically polarized incident plane wave ($E_\theta = 0$), and at frequency 8 GHz

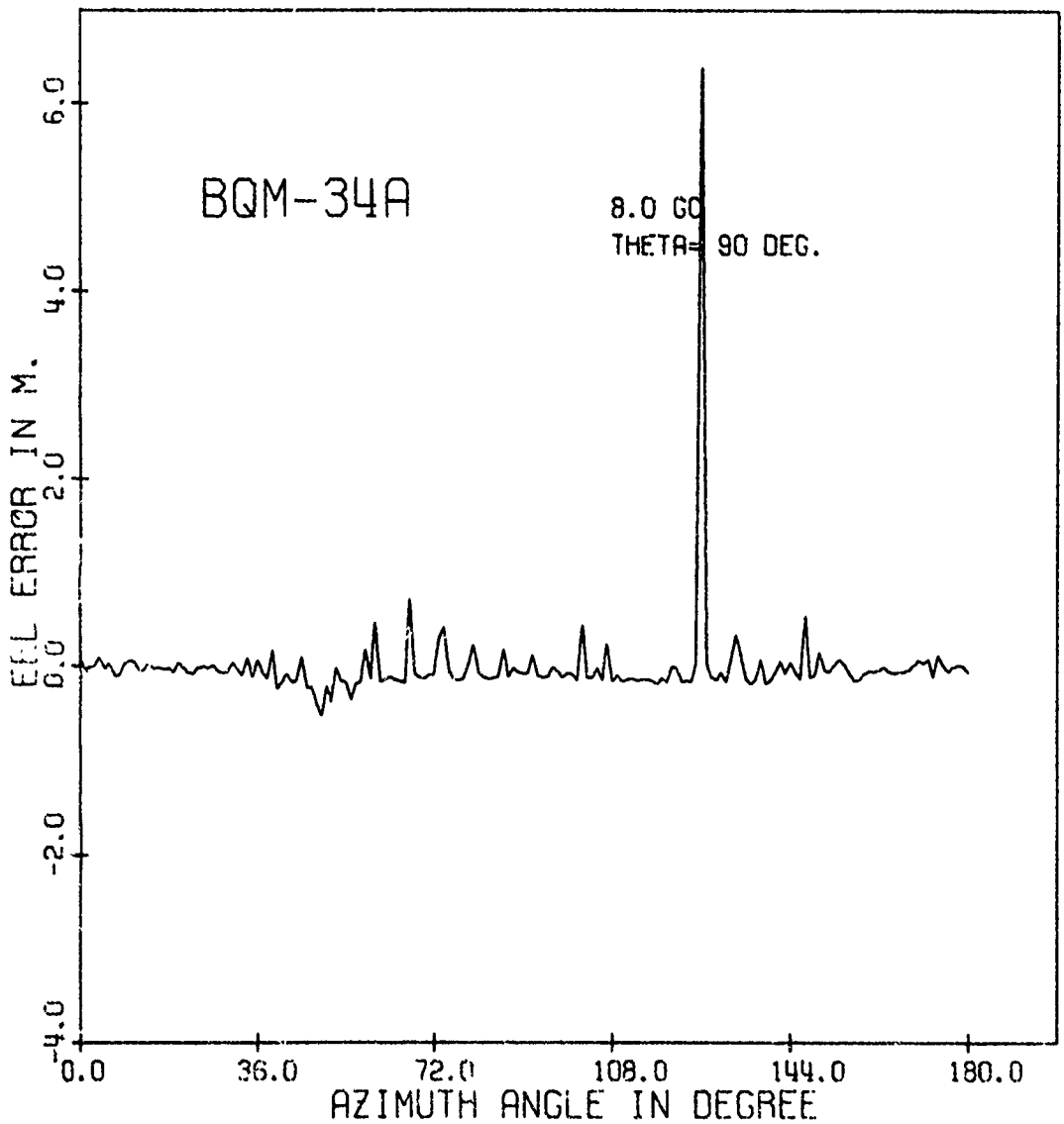

Figure 5.18. Elevation error (e_θ) in meters of the BQM-34A drone as a function of azimuth angle ϕ for a fixed $\theta = 90^\circ$, for a vertically polarized incident plane wave ($E_\theta = 0$), and at frequency 8 GHz

6. CONCLUSION

In this work, we have derived a relatively simple and analytical model for a complex airborne target. The results for the radar scattering parameters, i.e., RCS and angular scintillation, are given in terms of explicit simple functions and therefore can be calculated in an efficient manner with the aid of a computer. To test the accuracy of our model, the theoretical results are compared with the experimental data for T-33 aircraft. The agreement is generally good (within several db) except in the head-on and tail-on directions. In these two direction, our simple model using a semi-infinite cylinder with an ogive as the engine termination to approximate the engine duct is not adequate; and future work to develop a more realistic model is needed.

REFERENCES

[1] J.R.Crispin and K.M. Siegel, editors, Method of Radar Cross Section Analysis, New York: Academic Press, 1968.

[2] J.W. Wright, "On the Statistical Modeling of Radar Targets," Doctoral Thesis, University of Illinois, 1972; also presented at 1972 NEC, Chicago, Ill.

[3] J.J. Bowman, Senior, T.B.A. and P.L.E Uslenghi, editors, Electromagnetic and Acoustic Scattering by Simple Shapes, Amsterdam: North-Holland Publishing Co., 1969.

[4] J.B. Keller, "Geometrical Theory of Diffraction," J. of Opt. Soc. of Am., vol. 52, no. 2, pp. 116-130, February 1962.

[5] J.B. Keller, "Diffraction by an Aperture," J. of Appl. Phys., vol.28, no. 4, pp. 426-444, April 1957.

[6] P.L.E. Uslenghi and S.W. Lee, "High-Frequency Backscattering from an Elliptical Metal Plate," Antenna Lab Report No. 72-6, University of Illinois, 1972.

[7] E. F. Knott, Senior, T.B.A., and P.L.E. Uslenghi, "High-Frequency Back-scattering from a Metallic Disk," Proc. IEE, vol. 118, pp. 736-742, 1971.

[8] T.B.A. Senior, and P.L.E., "High-Frequency Backscattering from a Finite Core," Radio Science, vol. 6, no. 3, pp. 393-406, March 1971.

[9] E.F. Knott, Senior, T.B.A., and P.L.E. Uslenghi, "High-Frequency-Back-scattering from a Metallic Disk," Proc. IEE (London), vol. 118, pp. 736-742, 1971.

[10] M.E. Bechtel, "Application of Geometric Diffraction Theory to Scattering from Cones and Discs," Proc. IEEE, vol. 53, pp. 877-882, August 1965.

[11] R.A. Ross, "Radar Cross Section of Rectangular Flat Plates as a Function of Aspect Angle," Trans. IEEE, AP-14, May 1966.

[12] J.B. Keller, "Diffraction by an Aperture II," J. of Appl. Phys., vol. 28, no. 5, pp. 560-579, May 1957.

[13] D.S. Ahluwalia, R.M. Lewis, and J. Boersma, "Uniform Asymptotic Theory of Diffraction by a Plane Screen," SIAM J. Appl. Math., vol. 16, no. 4, pp. 783-807, July 1968.

[14] D. Ludwig, "Uniform Asymptotic Expansions of a Caustic," Commu. of Pure Appl. Math, vol. 19, pp. 245-250, 1966.

[15] B. Noble, "Reduction of the Integral Equations for High Frequency Diffraction by Disks and Strips," IRE Trans. on AP, pp. 537-542, December 1959.

[16] R.N. Buchal and J.B. Keller, "Boundary Layer Problems in Diffraction Theory," Commu. Pure Appl. Math, 13, pp. 85-114, 1960.

[17] R.G. Kouyoumjian, "Asymptotic High-Frequency Method," Proc. of the IRE , pp. 864-875, August 1965.

[18] C. Flammer, "The Vector Wave Function Solution of the Diffraction of Electromagnetic Waves by Circular Disks and Apertures, II - The Diffraction Problem," J. of Appl. Phys., vol. 14, No. 9, pp. 1224-1231, September 1953.

[19] E. Wolf and E.W. Marchand, "Comparison of the Kirchhoff and the Rayleigh-Sommerfeld Theories of Diffraction at an Aperture," J. Opt. So. Am., vol. 54, no. 5, pp. 587-594, May 1964.

[20] S.W. Lee, "Ray Theory of Diffraction by Open-Ended Waveguides, I. Field in Waveguides," J. Math. Phys., vol. 11, no. 9, pp. 2830-2850, September 1970.

[21] S.W. Lee, "Ray Theory of Diffraction by Open-Ended Waveguides II. Applications," J. Math. Phys., vol. 13, no. 5, pp. 656-664, May 1972.

[22] L.B. Felsen and H.Y. Yee,"Ray-Optical Techniques for Waveguide Discontinuities," IEEE Trans., vol.AP-16, pp. 268-269, 1968.

[23] G.T. Ruck, editor, Radar Cross Section Handbook, vol. 1 and vol. 2, New York: Plenum Press, 1970.

[24] J.R. Crispin and A.L. Mafett, "Radar Cross-Section Estimation for Complex Shapes," Proc of the IEEE, Special issue on Radar Reflectivity, pp. 972-982, August 1965.

[25] R.A. Ross and H.R. Witt, "Investigation of Scattering Center Theory," Interim Tech. Rep. UA-2462-E-1, Cornell Aeronautical Laboratory, 1967.

[26] J.W. Moll, and R.G. Seecamp, "Calculation of Radar Reflecting Properties of Jet Engine Intakes Using a Waveguide Model," IEEE Trans. vol. AES-6, no. 5, pp. 675-683, September 1970.

[27] P.H. Pathak and P.G. Kouyoumjian, "The Dyadic Diffraction Coefficient For a Perfectly Conducting Wedge," Technical Report 2183-4, ElectroScience Lab, The Ohio State U, 1970.

[28] J.H. Dunn, D.D. Howard, and A.M. King, "Phenomena of Scintillation Noise in Radar-Tracking System," Proc. IRE, vol. 47, pp. 855-863, May 1959.

[29] D.D. Howard, "Radar Target Angular Scintillation in Tracking and Guidance Systems Based on Echo Signal Phase Front Distortion," Proc. NEC, vol. 15, pp. 840-849, October 1959.

[30] J.J. Bowman, "Comparison of Ray Theory with Exact Theory for Scattering by Open Wave Guides," SIAM J. Appl. Math., vol. 18, no. 14, pp. 818-829, June 1970.

[31] R. Mittra and S.W. Lee, Analytic Methods in the Theory of Guided Waves, New York: Macmillan Co, 1970

[32] B. Noble, Methods Based on Wiener-Hopf Technique. New York: Pergamon Press, 1958.

[33] W.A. Pierson and R.W. Clay, "T-33 Radar Cross Section Measurements and Scintillation Analysis," RADC-TR-72-30, Final Technical Report, February 1972.

APPENDIX

A.1 Diffraction Matrix for a Wedge

Consider a perfectly conducting wedge of half-angle Ω whose edge coincides with the z axis of a Cartesian coordinate system (x, y, z) and whose surfaces are defined by the equations $y = \pm x \tan \Omega$, $x \geq 0$, and $-\infty < Z < \infty$. The geometry of the wedge is shown in Figure A.1.1. The problem of a plane wave incident or on a plane perpendicular to the Z axis with either its electric or magnetic vector parallel to the edge is a classic one; the exact solution is known, and from the basic results it is a trivial matter to deduce the corresponding solutions for plane waves incident at an angle $\pi-\beta$ to the Z axis.

According to Keller's geometrical theory of diffraction, we define a set of edge fixed base vectors $\hat{T}$, $\hat{N}$, and $\hat{B}$, where $\hat{T}$ is a unit vector parallel to the edge, $\hat{N}$ is a unit vector normal to the edge and pointing away from the wedge, and $\hat{B}$ is the unit vector binormal to the edge and pointing into the shadowed half space. The direction of $\hat{T}$ is chosen such that $\hat{T} = \hat{N} \times \hat{B}$ in a right-handed system. In general, we choose

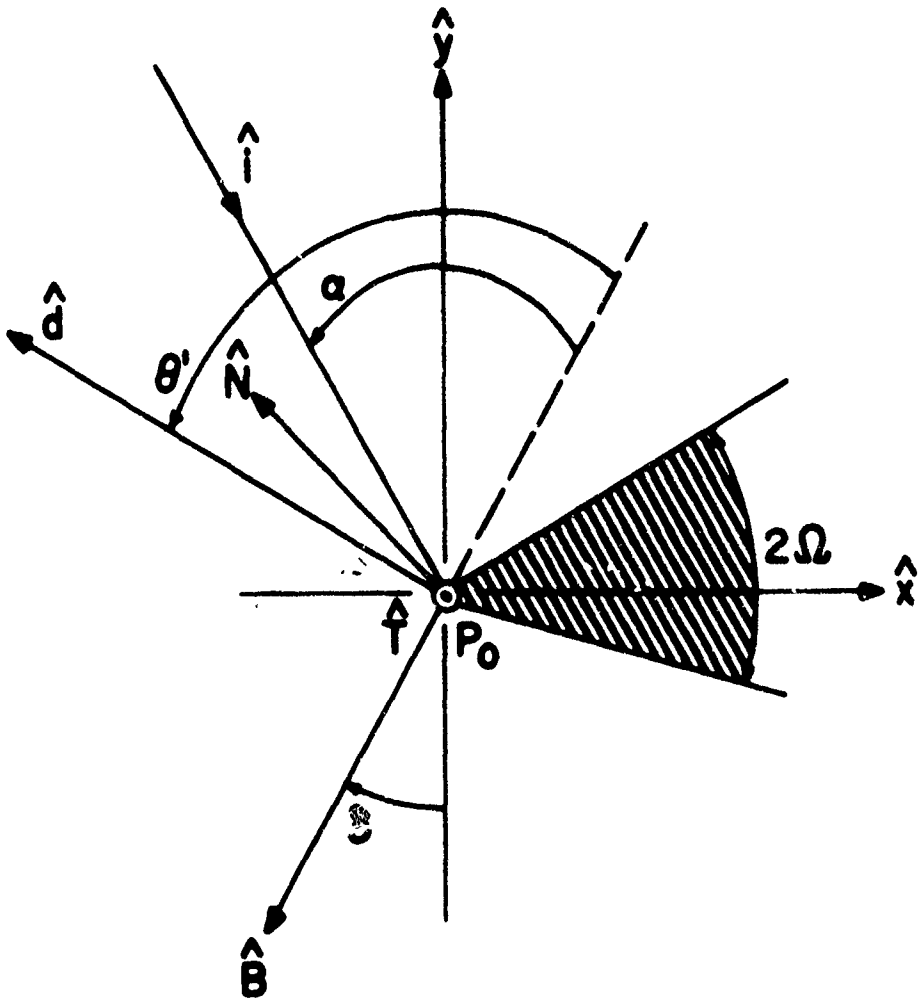

Figure A.1.1. The geometry of the wedge

$$\hat{T} = \hat{Z}$$

$$\hat{N} = -\hat{x} \cos \delta + \hat{y} \sin \delta \qquad \text{(A.1.1)}$$

$$\hat{B} = -\hat{x} \sin \delta - \hat{y} \cos \delta$$

where δ is arbitrary (see Figure A.1.1). If the incident field is

$$\bar{E}^i = \hat{e}^i \exp(i \vec{k}_1 \cdot \vec{r}) \qquad \text{(A.1.2)}$$

the diffracted electric field at points far from the edge and away from all geometrical optics boundaries can be written as

$$\bar{E}^d = \hat{e}^d \left\{ \frac{\exp[i(\pi/4)]}{\sin \beta (2\pi kr)^{1/2}} \right\} \exp(ik\hat{d} \cdot \vec{r}) \qquad \text{(A.1.3)}$$

where β is the angle between $\hat{T}$ and incident direction $\hat{i}$, r is the distance from the point of diffraction on the edge to the observation point, and k is the wave number. The incident and diffracted rays are on opposite sides of the plane which is normal to $\hat{T}$ and which contains the diffraction point P_0; their projections on this plane form angles α and θ' with $-\hat{B}$ (see Figure A.1.1) where

$$-(\pi/2) + \Omega + \delta \leq \alpha \leq (\pi/2) + \delta$$

$$-(\pi/2) + \Omega + \delta \leq \theta' \leq (3\pi/2) - \Omega + \delta$$

$$0 < \beta < \pi \quad . \qquad \text{(A.1.4)}$$

The vectors $\hat{e}^i$ and $\hat{e}^d$ are related by

$$\hat{e}^d = \Delta \hat{e}^i \qquad \text{(A.1.5)}$$

where

$$\Delta = -\begin{pmatrix} -(x - y) & & \\ (x - y)\cot\beta \sin\theta' & (x + y)\cos\theta'\cos\alpha & (x + y)\cos\theta'\sin\alpha \\ -(x - y)\cot\beta\cos\theta' & (x + y)\sin\theta'\cos\alpha & (x + y)\sin\theta'\sin\alpha \end{pmatrix}$$

$$\text{(A.1.6)}$$

$$x = \frac{1}{n}\sin\frac{\pi}{n}\left[\cos\frac{\pi}{n} - \cos\frac{1}{n}(\alpha + \theta')\right]^{-1}$$

$$y = \frac{1}{n}\sin\frac{\pi}{n}\left[\cos\frac{\pi}{n} + \cos\frac{1}{n}(\pi + 2\delta - \alpha - \theta')\right]^{-1} \qquad \text{(A.1.7)}$$

with

$$n = 2(1 - \frac{\Omega}{\pi}) \quad . \qquad \text{(A.1.8)}$$

Both $\hat{e}^i$ and $\hat{e}^d$ are column vectors with components along the base vectors $\hat{T}$, $\hat{N}$, and $\hat{B}$.

A.2 Diffraction Matrix for a Thin Edge

The perfectly conducting half plane shown in Figure A.2.1 is a special case of the wedge in Figure A.1.1, with half-angle Ω equal to zero. We define the base vectors $\hat{T}$, $\hat{N}$, and $\hat{B}$ as shown in Figure A.2.1.

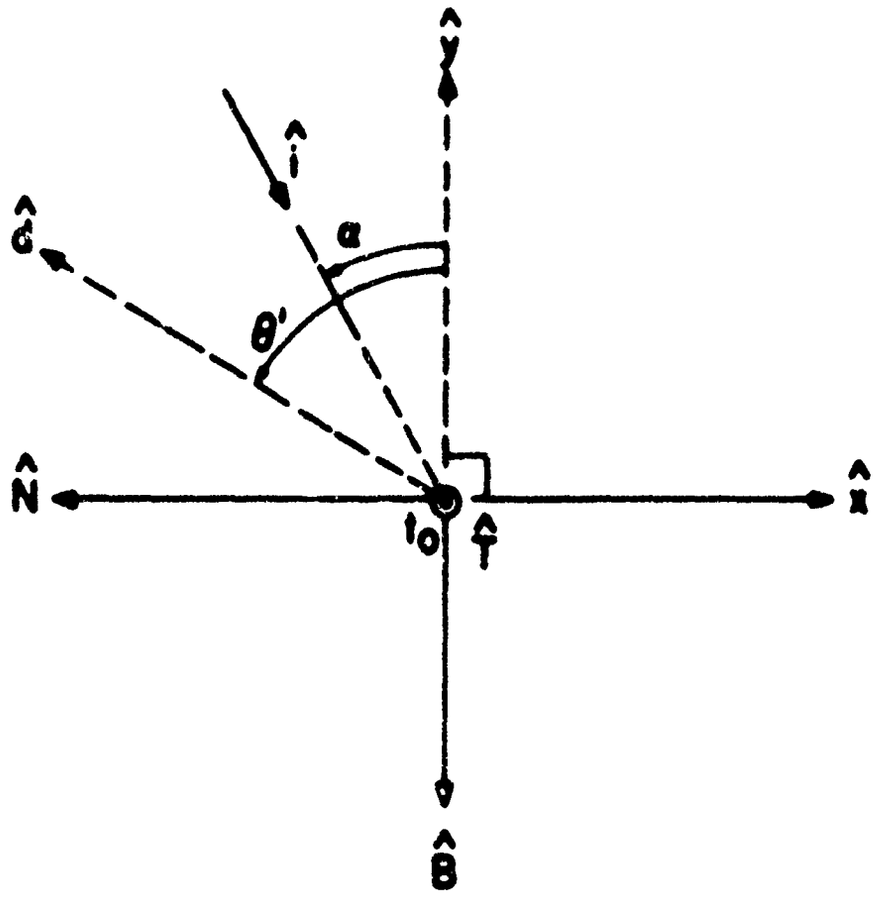

Figure A.2.1. Geometry for the plane diffraction

The incident and diffracted field can be written in the form of Equation (A.1.2) and Equation (A.1.3). The vectors $\hat{e}^i$ and $\hat{e}^d$ are related by

$$\hat{e}^d = \Delta \hat{e}^i \qquad \text{(A.2.1)}$$

where

$$\Delta = \begin{pmatrix} -(-x + y) & & \\ (-x + y) \cot \beta \sin \theta' & (-x - y) \cos \theta' \cos \alpha & (-x - y) \cos \theta' \sin \alpha \\ (-x + y) \cot \beta \cos \theta' & (-x - y) \sin \theta' \cos \alpha & (-x - y) \cos \theta' \sin \alpha \end{pmatrix} \qquad \text{(A.2.2)}$$

with

$$-\frac{\pi}{2} \leq \alpha \leq \frac{\pi}{2}$$

$$-\frac{\pi}{2} \leq \theta' \leq \frac{3\pi}{2} \quad . \qquad \text{(A.2.3)}$$

If the observation point p is not near the boundary of the shadow region, where $\theta' = \alpha + \pi$, i.e., if

$$\left|\cos \frac{\theta' - \alpha}{2}\right| \sqrt{2kr \sin \beta} \gg 1 \ , \qquad \text{(A.2.4)}$$

then

$$y \approx \frac{1}{2 \cos \frac{\theta' - \alpha}{2}} \quad . \tag{A.2.5}$$

If p is not near the boundary of the reflected field, where $\theta' \approx -\alpha$, i.e., if

$$\left| \sin \frac{\theta' + \alpha}{2} \right| \sqrt{2kr \sin \beta} \gg 1 \ , \tag{A.2.6}$$

then

$$x \approx \frac{1}{2 \sin \frac{\theta' + \alpha}{2}} \quad . \tag{A.2.7}$$

A.3 The Divergence Factor for the Diffracted Ray from a Curved Edge

By applying the geometry theory of diffraction, the divergence factor for the diffracted field from a curved edge can be written as

$$\Gamma = \left[\frac{\rho}{(\rho + S)S} \right]^{1/2} \tag{A.3.1}$$

where ρ is the principal radius of curvature of the wave fronts diffracted by the edge and S is the distance from the edge to the observation point. The radius of curvature of the wavefront is

$$\rho = \frac{-\rho' \sin^2 \beta}{(\hat{d} - \hat{i}) \cdot \vec{n}} \qquad \text{(A.3.2)}$$

where ρ' is the radius of curvature of the edge, β is the angle between the incident ray and the tangent to the edge, $\hat{d}$ is the unit vector in the direction of the diffracted ray, and $\hat{n}$ is the unit vector in the direction of the principal normal to the edge.

The principal normal to an edge is the normal lying in a plane containing the edge at the location of interest.